LEBANESE AMERICAN UNIVERSITY

An eddy viscosity PANS model for non-zonal continuous hybrid RANS/LES simulations

By

Maher Eid

A thesis

submitted in partial fulfillment of the requirements

for the degree of Master of Science in Mechanical Engineering

School of Engineering

May 2022

LAU
الجامعة اللبنانية الأميركية
Lebanese American University

THESIS APPROVAL FORM

Student Name: Maher Eid I.D. #: 201405102

Thesis Title : An eddy viscosity PANS model for non-zonal continuous hybrid RANS/LES simulations

Program: MS in Mechanical Engineering

Department: Department of Industrial and Mechanical Engineering

School: School of Engineering

The undersigned certify that they have examined the final electronic copy of this thesis and approved it in Partial Fulfillment of the requirements for the degree of:

Master of Science in the major of Mechanical Engineering

Thesis Advisor's Name Michel Elkhoury	Signature [redacted]	DATE: 10 / 05 / 2022 (Day / Month / Year)
Committee Member's Name Amne El Cheikh	Signature [redacted]	DATE: 08 / 05 / 2022 (Day / Month / Year)
Committee Member's Name Nader El Khatib	Signature [redacted]	DATE: 13 / 05 / 2022 (Day / Month / Year)

LAU
الجامعة اللبنانية الأميركية
Lebanese American University

THESIS COPYRIGHT RELEASE FORM

LEBANESE AMERICAN UNIVERSITY NON-EXCLUSIVE DISTRIBUTION LICENSE

By signing and submitting this license, you (the author(s) or copyright owner) grants the Lebanese American University (LAU) the non-exclusive right to reproduce, translate (as defined below), and/or distribute your submission (including the abstract) worldwide in print and electronic formats and in any medium, including but not limited to audio or video. You agree that LAU may, without changing the content, translate the submission to any medium or format for the purpose of preservation. You also agree that LAU may keep more than one copy of this submission for purposes of security, backup and preservation. You represent that the submission is your original work, and that you have the right to grant the rights contained in this license. You also represent that your submission does not, to the best of your knowledge, infringe upon anyone's copyright. If the submission contains material for which you do not hold copyright, you represent that you have obtained the unrestricted permission of the copyright owner to grant LAU the rights required by this license, and that such third-party owned material is clearly identified and acknowledged within the text or content of the submission. IF THE SUBMISSION IS BASED UPON WORK THAT HAS BEEN SPONSORED OR SUPPORTED BY AN AGENCY OR ORGANIZATION OTHER THAN LAU, YOU REPRESENT THAT YOU HAVE FULFILLED ANY RIGHT OF REVIEW OR OTHER OBLIGATIONS REQUIRED BY SUCH CONTRACT OR AGREEMENT. LAU will clearly identify your name(s) as the author(s) or owner(s) of the submission, and will not make any alteration, other than as allowed by this license, to your submission.

Name: Maher Eid

Signature: [redacted]

Date: 13-May-2022

LAU
الجامعة اللبنانية الأميركية
Lebanese American University

PLAGIARISM POLICY COMPLIANCE STATEMENT

I certify that:

1. I have read and understood LAU's Plagiarism Policy.
2. I understand that failure to comply with this Policy can lead to academic and disciplinary actions against me.
3. This work is substantially my own, and to the extent that any part of this work is not my own I have indicated that by acknowledging its sources.

Name: Maher Eid

Signature: [redacted]

Date: 13-May-2022

iv

Acknowledgment

I would like to thank everyone who has helped and supported me in preparing and submitting this thesis. First of all, I would like to express my gratitude to my graduate advisor Dr. Michel Khoury who has been a great teacher, advisor, and mentor. His teaching and guidance had an immense impact on this work and on me personally becoming a better scholar. Also, I would like to thank the engineering lab staff at the Lebanese American University, especially Mr. Salim Jamal-Eddine, who has been always ready and available to fix all the technical issues I have encountered. I also thank the teaching faculty of the Industrial and Mechanical Engineering department for their courses and guidance throughout my undergraduate and graduate studies. I would like to extend my gratitude to my colleagues and friends who have supported me during the final period of my studies. Finally, I would like to thank the Lebanese American University for providing me with the licenses and computational power needed. Without them, this work would not have been possible.

An eddy viscosity PANS model for non-zonal continuous hybrid RANS/LES simulations

Maher Eid

ABSTRACT

The extremely stringent requirement of fully resolving turbulence in Direct Numerical Simulation (DNS) of fluid flows has forced researchers and engineers to rely heavily on averaged methods like the Reynolds' Averaged Navier-Stokes (RANS) for common engineering applications. The process of averaging in RANS results in the full spectrum of turbulent scales being fully modeled instead of resolved as in DNS. This comes at a cost of lower accuracy and reliability, which could have adverse effects on the design or research at hand. With the current computer technology barely keeping up with Moore's law, it is expected that we are decades away from having enough computing power to make DNS a feasible option outside purely academic settings. The huge gap between RANS and DNS has led to the development of hybrid models that offer the benefits of both extremes, by allowing part of turbulence to be exactly resolved, thus reducing the inaccuracies associated with the smaller modeling part. Partially Averaged Navier-Stokes (PANS) bridges between RANS and DNS, providing the adequate balance between modeled and resolved quantities. In this study, a new PANS model based on the one-equation transport of the unresolved turbulent eddy viscosity ν_{tu} is proposed. This is, to the author's knowledge, the first PANS model in which the resolution level is controlled by the ratio of unresolved-to-total turbulent eddy viscosity f_{ν_t}. In addition, f_{ν_t} is both a spatially and temporally varying quantity derived directly from the integration of the energy density spectrum. This gives the proposed model a more physically sound formulation, compared to the empiricism and ad-hoc shielding usually used in hybrid models. Two val-

idation test cases are investigated, with the first involving shear flow between a moving and stationary fluid i.e., the backward-facing step, and the external aerodynamic flow over a simplified car body, i.e., the Ahmed body. Both cases are simulated using the proposed model, Improved Delayed Detached Eddy Simulation (IDDES), and Wall Modeled Large Eddy Simulation (WMLES). The latter two models are also scale-resolving methods used for comparison in the current study. Validation of the results are performed against data from well-established experimental setups. The proposed PANS model shows higher accuracy in predicting the average velocity profiles, as well as the turbulent stresses in the backward-facing step compared to IDDES and WMLES. In addition, PANS is able to release more structures than the other models for the same grid density, showing that strong shielding is not always an advantage. For external aerodynamics applications, i.e., the Ahmed Body, PANS shows better drag predictions with levels of turbulent stresses comparable to IDDES. With the given grid of this case, PANS is able to automatically adjust the level of resolution to cover upstream locations with a fully modeled formulation, and switch to a more resolving one on the slant and downstream the body. Overall, the proposed PANS model shows promising results in this preliminary study.

Keywords: Turbulence modelling, Partially Averaged Navier-Stokes, Scale-Resolving methods, Hybrid RANS/LES, Backward-facing step, Ahmed body.

Table of Contents

1 Introduction **1**

1.1 Hybrid Modelling 3

1.2 Thesis Aims and Objectives 5

1.3 Thesis Outline 6

2 Model Development **7**

2.1 PANS Governing Equations 7

2.2 Modelling the f_{ν_t} parameter 9

2.3 Relationship to the Smagorinsky model 15

3 Numerical Method **17**

3.1 Numerical Considerations 17

3.2 User Defined Function (UDF) 18

3.3 Wall Modeled Large Eddy Simulation 20

3.4 Improved Delayed Detached Eddy Simulation 22

4 Cases Setup **24**

4.1 Backward-Facing Step 24

4.2 Ahmed Body 26

5 Results and Discussion **30**

5.1 Backward-Facing Step 30

5.1.1 Sampling Time 30

5.1.2 Mesh study and model validation 33

5.2 Ahmed Body 53

5.2.1 Sampling Time 53

5.2.2 Model Validation 53

6 Conclusion **62**

References **63**

List of Tables

Table 1 Grid distributions for the 3 meshes of the backward-facing step 26

Table 2 Convergence of reattachment length for the PANS fine case 32

Table 3 Reattachment Length X_R/H 35

Table 4 Lift and Drag coefficients on the Ahmed body 55

List of Figures

Figure 1 Turbulent energy density spectrum 2

Figure 2 Zonal and non-zonal methods 4

Figure 3 f_k distributions against the non-dimensional length scale Λ/Δ 11

Figure 4 f_{ν_t} distributions against the non-dimensional length scale η_{tu} 14

Figure 5 Backward-facing step computational domain geometry . . 25

Figure 6 Grids of the backward-facing step. From top to bottom: Coarse, Medium, and Fine mesh 26

Figure 7 Reference sketches of the Ahmed body 27

Figure 8 Mesh around the Ahmed body 28

Figure 9 Mesh around the Ahmed body zoomed in on the slant . . . 29

Figure 10 Convergence of mean skin friction coefficient for the PANS fine case 32

Figure 11 Convergence of velocity and turbulent shear stresses for the PANS fine case at x = 1H 33

Figure 12 Convergence of velocity and turbulent shear stresses for the PANS fine case at x = 10H 34

Figure 13 Mean skin friction coefficient distributions of PANS 35

Figure 14 Mean skin friction coefficient distributions of IDDES . . . 36

Figure 15 Mean skin friction coefficient distributions of WMLES . . . 37

Figure 16 Reattachment length for the backward-facing step 37

Figure 17 Mean skin friction coefficient for the various models on the coarse grid 38

Figure 18 Mean skin friction coefficient for the various models on the medium grid 39

Figure 19 Mean skin friction coefficient for the various models on the fine grid 40
Figure 20 Mean streamwise velocity profiles on the coarse mesh (contours are shown for PANS) 42
Figure 21 Turbulent normal stress profiles on the coarse mesh (contours are shown for PANS) 43
Figure 22 Turbulent shear stress profiles on the coarse mesh (contours are shown for PANS) 44
Figure 23 Mean streamwise velocity profiles on the medium mesh (contours are shown for PANS) 45
Figure 24 Turbulent normal stress profiles on the medium mesh (contours are shown for PANS) 46
Figure 25 Turbulent shear stress profiles on the medium mesh (contours are shown for PANS) 47
Figure 26 Mean streamwise velocity profiles on the fine mesh (contours are shown for PANS) 48
Figure 27 Turbulent normal stress profiles on the fine mesh (contours are shown for PANS) 49
Figure 28 Turbulent shear stress profiles on the fine mesh (contours are shown for PANS) 50
Figure 29 Velocity contours on isosurfaces of $Q = 1e^5$ for PANS (left), IDDES (middle), and WMLES (right) for the low density mesh . 51
Figure 30 Velocity contours on isosurfaces of $Q = 1e^5$ for PANS (left), IDDES (middle), and WMLES (right) for the medium density mesh 51
Figure 31 Velocity contours on isosurfaces of $Q = 1e^5$ for PANS (left), IDDES (middle), and WMLES (right) for the high density mesh . 52
Figure 32 Convergence of velocity and streamwise velocity fluctuations for x = -0.012m 54

Figure 33 Convergence of velocity and streamwise velocity fluctuations for x = 0.038m 55
Figure 34 Profiles of the average streamwise velocity U over the Ahmed body 56
Figure 35 Profiles of the average wall normal velocity W over the Ahmed body 56
Figure 36 Profiles of the average streamwise velocity fluctuations $u - rms$ over the Ahmed body 57
Figure 37 Profiles of the average wall normal velocity fluctuations $w - rms$ over the Ahmed body 57
Figure 38 Contours of the average streamwise velocity U. From left to right: Exp., WMLES, IDDES, and PANS. 58
Figure 39 Contours of the average spanwise velocity V. From left to right: Exp., WMLES, IDDES, and PANS. 59
Figure 40 Contours of the average wall normal velocity W. From left to right: Exp., WMLES, IDDES, and PANS. 60
Figure 41 Contours of the average streamwise velocity fluctuations u-rms. From left to right: Exp., WMLES, IDDES, and PANS. . . 60
Figure 42 Contours of averaged wall shear stresses on the Ahmed body 61
Figure 43 Isosurfaces of Q-criterion with contours of velocity magnitude 61

Chapter One

Introduction

Turbulence remains one of the major sources of inaccuracies in the computation of fluid flows. The onset of turbulent behavior is dictated by the ratio of inertial to viscous forces, defined by the Reynolds' number (Re). If this number exceeds some critical value, velocity fluctuations become strong enough to sustain the production and transport of turbulent swirls or "eddies" spanning over a wide range of scales. The larger the Reynolds' number gets, the wider the range becomes. The turbulent energy of the flow is distributed among these scales, with every eddy having an energy density E(κ) related to its wavenumber κ (inversely related to the eddy diameter). The distribution of E(κ) is plotted in Figure 1 against the wavenumber κ. According to this plot, the biggest eddies (smallest κ), which are comparable in size to the characteristic length of the geometry, bear most of the turbulent energy in the spectrum. These eddies eventually weaken and break, transferring their energies to smaller ones, which in turn carry on the same function all the way to the smallest scales as depicted in Figure 1. At the end of the spectrum, the energy of the smallest eddies (largest κ) is so low that molecular viscosity dissipates them in the form of heat. Thus, these scales are referred to as the dissipative scales, making up the viscous range. Between the energy containing range and the viscous range, the energy density has a linear trend when plotted on a logarithmic scale. The slope was found to be equal to -5/3 by Kolmogorov (1968). This range is commonly referred to as the inertial range. All of the physics involved in turbulence, including the part discussed above, is captured in the full Navier-Stokes flow equations. To simulate turbulent flows in an exact manner, i.e., numerically solving the governing Navier-Stokes equations, all scales in the turbulent spectrum must be accurately resolved. Such a process is referred to as Direct Numerical Simulation (DNS).

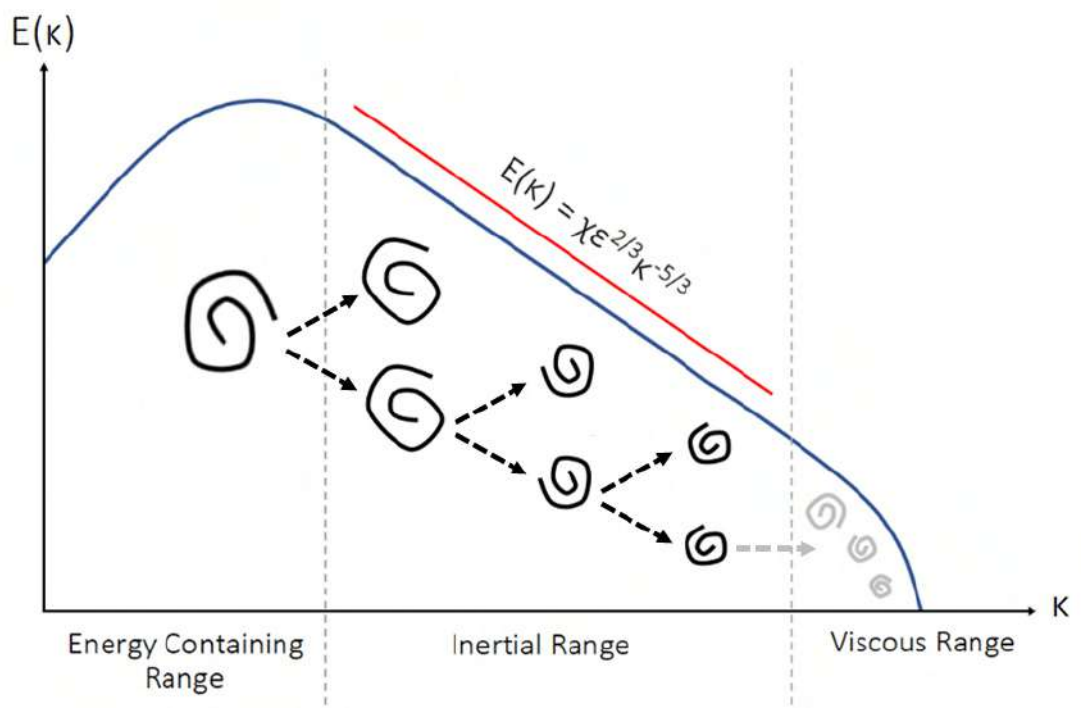

Figure 1: Turbulent energy density spectrum

However, due to the wide energy spectrum, such endeavor requires a mesh fine enough to capture the smallest dissipative scales, making the number of elements needed grow proportionally to $Re^{9/4}$ (Chaouat, 2017). This renders the use of DNS in common engineering applications extremely expensive or in some cases prohibitive with the current computer technology. On the other hand, the increasing reliance on numerical simulations in both academic and industrial fields, has led to the development of several methods to overcome the cost of performing DNS even when accuracy could potentially be compromised. Most quantities of interest in engineering designs are averaged values i.e., shear, lift, and drag forces to name a few. An alternative to DNS capable of yielding such quantities consists of directly averaging the instantaneous N-S equations over large periods of time compared to the turbulent time scales, in the spirit of computing the correct averaged velocity fields. This approach is known as the Reynolds Averaged Navier-Stokes equations (RANS) and its main goal is to model all the turbulent scales instead of resolving them like in DNS. Such mathematical endeavor i.e., averaging non-linear terms, results in some additional unclosed quantities in the

averaged equations termed the Reynolds' stresses. These stress terms can then be modelled by a variety of RANS methods (algebraic, 1 equation, 2 equations, etc.). The computational requirements of RANS are thereby much lighter and independent of Re (Chaouat, 2017). The main problem with RANS models is their inherent lack of accuracy due to the modelling of the new stress terms. The deficiencies of RANS are further increased when separation, curvature, and other effects are present. This is of course in addition to the assumptions made and the empirical calibration. The computationally expensive, yet accurate DNS, and the cheap questionable RANS represent the two extremes of turbulence modelling. To get the best of both worlds, scale-resolving methods were developed to resolve the large scales containing most of the flow turbulent energy, while modelling the smaller ones. Large Eddy Simulation (LES) does exactly that by filtering the Navier-Stokes equations. However, the problem with LES is that the largest scales near walls (i.e., inside the boundary layer) remain small enough to be accurately resolved, resulting in a mesh that is comparable in size to DNS at such locations. This, in a way compromises the use of LES in common engineering applications where physical walls are important features of the problem, like for example in turbines, pumps, wings, etc.

1.1 Hybrid Modelling

To alleviate some of the computational requirements of LES i.e., the near wall grid resolution, hybrid models are designed to solve a combination of RANS and LES equations. These hybrid methods are most commonly categorized as either zonal or non-zonal approaches as will be described below. In zonal approaches, the domain is divided into several regions, where the full RANS equations are solved in some, while LES equations are solved in the elsewhere. This results in a sharp interface between such regions as seen in the left part of Figure 2. It is worthy to note that this interface is not necessarily fixed and can be a dynamic

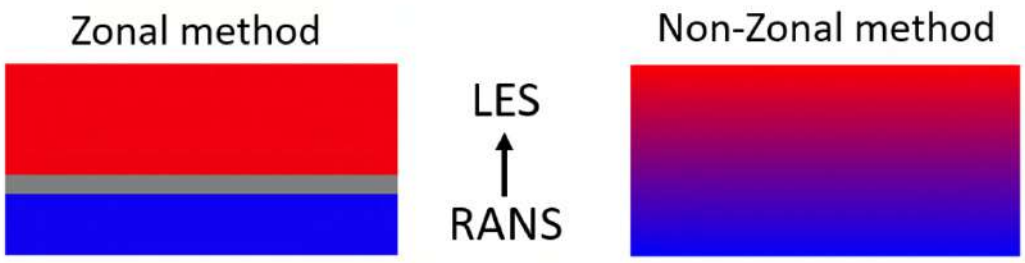

Figure 2: Zonal and non-zonal methods

one depending on the method used and the flow evolution. It is however essential, that the separation between different regions is always clear in order to solve the appropriate set of equations where needed. An example of a zonal approach is the Detached Eddy Simulation (DES) proposed by Spalart et al. (1997). In DES, LES equations are solved in the free-shear regions where turbulent scales are relatively large, while RANS is used in the near-wall boundary layer, allowing the use of a coarser grid at such locations. Zonal approaches were proven to have some issues, namely, choosing adequate criteria to separate different regions and properly modelling the interaction between the two models at the RANS-LES interfaces commonly referred to as the grey area (Chaouat, 2017). The DES for example, suffers mostly from the first issue, where the model could switch to an LES formulation with a grid size not meeting the LES requirements. This is known as the Grid-Induced Separation (GID) and has been the subject of extensive development as will be shown in later sections, to provide better shielding, preventing LES from being solved inside any part of the boundary layer. In addition to this, correctly coupling the RANS and LES approaches at the interface to match the velocity profiles on both sides, requires special treatment. Synthetic turbulence generators are used to convert the modeled RANS content to the fluctuations needed for the LES equations. Again, this is one of major disadvantage of zonal methods. The alternative to zonal approaches in hybrid models consists of seamlessly switching from RANS to LES by bridging the two sets of equations without abrupt discontinuities at the interface (Speziale, 1998). As seen in the right part Figure 2, no clear separation is seen between the two

regions. This completely eliminates the need for synthetic turbulence generators as the model is now able to resolve part of the turbulence while going from a RANS to LES formulation. There are also several classes of models involving non-zonal approaches. The one investigated in this study consists of partially averaging the N-S equations, resulting in the Partially Averaged Navier-Stokes equation (PANS). PANS was initially proposed by Girimaji (2005) with the original model derived from a set of parent RANS $k-\epsilon$ equations. The formalism of such an approach is to transform the RANS equations of the total turbulent kinetic energy k and total dissipation of turbulent kinetic energy ϵ into equations for the unresolved ones, i.e., k_u and ϵ_u, respectively. Doing so results in two additional parameters, $f_k = k_u/k$ and $f_\epsilon = \epsilon_u/\epsilon$ designating the ratio of the unresolved-to-total turbulent kinetic energy and dissipation rate, respectively. When these ratios take the value of unity, the model recovers the original RANS formulation with all the turbulence being modelled (unresolved), and gradually goes to DNS when they go to zero. Initially, Girimaji (2005) used constant ratios for f_k and f_ϵ throughout the domain with promising prelminary results. Girmiaji and Abdol-Hamid (2005) then developed a more dynamic formulation allowing the ratio f_k to vary in space. It should be noted that any RANS model is a potential candidate for constituting a base model for the PANS equations. Reyes (2008) derived a PANS model using the original $k-\omega$ formulation. In the same spirit. Ma et al. (2011) used a Low Reynolds' Number LRN form of the $k-\epsilon$ while Huang et al. (2017) used a Modified $k-\omega$ SST model. The approaches look similar, yet only two-equation models seem to be the exclusive trend in PANS.

1.2 Thesis Aims and Objectives

This study will be based on the previous literature to propose a new Hybrid RANS/LES model, specifically PANS, for simulating turbulence. The main objective of this study is to resolve as much of the turbulent energy as possible with

the available grid size, while modelling the rest of the spectrum with a sub-grid one-equation model based on the ratio of unresolved-to-total turbulent viscosity f_{ν_t}. The proposed model uses a non-zonal approach, thus is able to seamlessly switch from RANS to LES. This is, to the author's knowledge, the first PANS model, to use a one-equation RANS model as the base model. Since f_{ν_t} will be a function of the PANS variable ν_{tu}, no RANS solution is needed prior to the calculations, and no averaging over the previous time steps is involved as in the previous models that depends on solving the turbulent scales. It is expected that the proposed model will have high accuracy in modelling turbulence compared to the available hybrid methods, at a lower computational cost than conventional techniques like LES and DNS.

1.3 Thesis Outline

In Chapter 2, the proposed PANS model is derived from the Menter one-equation RANS model based on the turbulent viscosity (1997). The resolution controlling parameter f_{ν_t} is also derived from mathematically and physically sound arguments. In Chapter 3, the numerical method and considerations are presented including the formulation of the source code used to implement the proposed model, as well as the other scale-resolving methods used for comparison. The numerical case setups are presented in Chapter 4 showing with great detail the domain and grid used for the computations. The results of the simulations are presented and discussed in Chapter 5. The study is concluded in Chapter 6 along with the recommendations.

Chapter Two

Model Development

2.1 PANS Governing Equations

The incompressible one-equation RANS model for the turbulent eddy viscosity developed by Menter (1997) is read as

$$\frac{\partial \nu_t}{\partial t} + \overline{U}_j \frac{\partial \nu_t}{\partial x_j} = D_1 c_1 S \nu_t + \frac{\partial}{\partial x_j}\left(\left(\nu + \frac{\nu_t}{\sigma}\right)\frac{\partial \nu_t}{\partial x_j}\right) - c_2 \frac{{\nu_t}^2}{{L_{vk}}^2} \tag{1}$$

With $\overline{U}_j$ being the RANS averaged velocity. D_1 is a damping function used for the low Reynolds' number form of the model, S is the mean strain rate, σ is the turbulent prandtl number, and L_{vk} is the von Karman length scale. The constants of the model take the values of $c_2 = 0.144$ and $c_2 = 0.186$.

For details about the derivation along with the formalism and assumptions of the above model, the reader is referred to the original paper (Menter, 1997). The motivation behind this study is to rewrite the previous RANS equation Eq.(1) in a PANS framework, thereby replacing the total turbulent viscosity ν_t by the unresolved one ν_{tu}. The resulting PDE should be of the following form

$$\frac{\partial \nu_{tu}}{\partial t} + U_j \frac{\partial \nu_{tu}}{\partial x_j} = P_u + T_u - D_u \tag{2}$$

where P_u, T_u, and D_u are the unresolved production, diffusion, and dissipation of unresolved turbulent viscosity, respectively. To quantify the degree of resolution, the ratio of unresolved-to-total turbulent viscosity f_{ν_t} is defined as

$$f_{\nu_t} = \frac{\nu_{tu}}{\nu_t} \tag{3}$$

Assuming a constant f_{ν_t} for now, that commutes with spatial and temporal derivatives, the equations are then transformed using

$$\frac{\partial \nu_{tu}}{\partial t} + \overline{U}_j \frac{\partial \nu_{tu}}{\partial x_j} = f_{v_t} \left(\frac{\partial \nu_t}{\partial t} + \overline{U}_j \frac{\partial \nu_t}{\partial x_j} \right) \tag{4}$$

Replacing the advection term of Eq.(4), i.e., $\left(\frac{\partial \nu_t}{\partial t} + \overline{U}_j \frac{\partial \nu_t}{\partial x_j} \right)$, by the RHS terms of Eq.(1) yields

$$\frac{\partial \nu_{tu}}{\partial t} + \overline{U}_j \frac{\partial \nu_{tu}}{\partial x_j} = f_{v_t} \left(D_1 c_1 S \nu_t + \frac{\partial}{\partial x_j} \left(\left(\nu + \frac{\nu_t}{\sigma} \right) \frac{\partial \nu_t}{\partial x_j} \right) - c_2 \frac{{\nu_t}^2}{{L_{vk}}^2} \right) \tag{5}$$

Adding $\left(U_j - \overline{U}_j \right) \frac{\partial \nu_{tu}}{\partial x_j}$ to both sides of Eq.(5) results in

$$\frac{\partial \nu_{tu}}{\partial t} + U_j \frac{\partial \nu_{tu}}{\partial x_j} = f_{v_t} \left(D_1 c_1 S \nu_t + \frac{\partial}{\partial x_j} \left(\left(\nu + \frac{\nu_t}{\sigma} \right) \frac{\partial \nu_t}{\partial x_j} \right) - c_2 \frac{{\nu_t}^2}{{L_{vk}}^2} \right) + \left(U_j - \overline{U}_j \right) \frac{\partial \nu_{tu}}{\partial x_j} \tag{6}$$

By comparing the terms of Eq.(6) to those of Eq.(2), the formulations of the production, destruction, and transport terms become

$$P_u = D_1 c_1 S \nu_{t_u} \tag{7}$$

$$D_u = f_{\nu_t} \frac{c_2}{f_{\nu_t}^2} \frac{\nu_{tu}^2}{L_{vk}^2} = \frac{c_2}{f_{\nu_t}} \frac{\nu_{tu}^2}{L_{vk}^2} \tag{8}$$

$$T_u = \frac{\partial}{\partial x_j} \left(\left(\nu + \frac{\nu_t}{\sigma} \right) \frac{\partial \nu_{tu}}{\partial x_j} \right) + \left(U_j - \overline{U}_j \right) \frac{\partial \nu_{tu}}{\partial x_j} \tag{9}$$

The term $\left(U_j - \overline{U}_j \right) \frac{\partial \nu_{tu}}{\partial x_j}$ in Eq.(9) represents the transport of unresolved turbulent viscosity by the resolved fluctuations. In order to close the PANS model, this term needs further modelling. Murthi (2004) proposed the maximum transport model stating that the resolved and unresolved fluctuations have proportional contributions to the transport of the unresolved scales. The level of contribution of each is in turn proportional to the eddy viscosity following $\nu_t = \nu_{tu} + \nu_{tr}$, where ν_{tr} is the resolved turbulent viscosity. The contribution of the resolved

fluctuations on the transport of unresolved scales becomes

$$-\left(U_j-\overline{U}_j\right)\frac{\partial \nu_{tu}}{\partial x_j}=\frac{\partial}{\partial x_j}\left(\left(\nu+\frac{\nu_{tr}}{\sigma}\right)\frac{\partial \nu_{tu}}{\partial x_j}\right) \tag{10}$$

Substituting the above term in Eq.(9) yields

$$T_u=\frac{\partial}{\partial x_j}\left(\left(\nu+\frac{\nu_{tu}}{\sigma}\right)\frac{\partial \nu_{tu}}{\partial x_j}\right) \tag{11}$$

The one-equation PANS model takes the following final form

$$\frac{\partial \nu_{tu}}{\partial t}+U_j\frac{\partial \nu_{tu}}{\partial x_j}=D_1c_1S\nu_{tu}+\frac{\partial}{\partial x_j}\left(\left(\nu+\frac{\nu_{tu}}{\sigma}\right)\frac{\partial \nu_{tu}}{\partial x_j}\right)-\frac{c_2}{f_{\nu_t}}\frac{{\nu_{tu}}^2}{{L_{vk}}^2} \tag{12}$$

2.2 Modelling the f_{ν_t} parameter

As demonstrated in the previous section, the parameter f_{ν_t} requires the knowledge of ν_t, which is the total resolved and unresolved turbulent eddy viscosity. In the Partially Integrated Transport Model (PITM) proposed by Schiestel and Dejoan (2005), the integration of the density spectrum function E(κ) has been used to estimate the ratio of unresolved to total kinetic energy as the following

$$f_k=\frac{k_u}{k}=\frac{\int_{\kappa_c}^{\infty}E(\kappa)d\kappa}{k_r+k_u}=\frac{\int_{\kappa_c}^{\infty}E(\kappa)d\kappa}{\int_0^{\infty}E(\kappa)d\kappa} \tag{13}$$

Here κ_c is the cutoff wavenumber, which is the spectral filter size and is related to the actual grid by $\kappa_c=\pi/\Delta$. The turbulent energy density spectrum as a function of wave number showing resolved and modeled scales is depicted in Figure 1. One accurate equation for E(κ) that maps the entire spectrum, which is similar to those proposed by Von Karman (Hinze, 1975), was used by Foroutan

and Yavuzkurt (2014) and may be defined by

$$E(\kappa) = \chi \epsilon^{2/3} \kappa^{\mu} \left[\left(\frac{\chi \epsilon^{2/3}}{C} \right)^{\frac{2}{3\mu+5}} + \kappa^{2/3} \right]^{-\frac{3\mu+5}{2}} \tag{14}$$

where C is a constant that can be obtained from $k = \int_0^{\infty} E(\kappa) d\kappa$ and χ is the Kolmogorov constant that is generally taken as 1.5. As can be noticed, at very low wavenumbers, i.e., $\kappa \approx 0$, Eq.(14) reduces to $E(\kappa) \approx C\kappa^{\mu}$ which resembles the situation of "permanence of big eddies" as referred to by Lesieur (2014). μ is another constant that normally ranges as $1 \leqslant \mu \leqslant 4$. The value of μ is debatable and subject to different interpretations, being integer, odd, even, or a non-integer one. Davidson (2000) recommends a value of 2 while Deardorff (1970) suggested a value of 4. Falkovich et. al. (2001) even recommended non-integer values. Schiestel and Dejoan (2005) used $\mu = 1.4$ that was derived using the standard $k - \epsilon$ closure's constants in a decaying homogeneous turbulence. The ratio of unresolved-to-total turbulent kinetic energy k_u/k can be calculated analytically by integrating the energy spectrum as follows

$$f_k = \frac{k_u}{k} = \frac{\int_{\kappa_c}^{\infty} E(\kappa) d\kappa}{k} = 1 - \left[\frac{\left(\frac{\kappa_c}{\kappa_{ref}} \right)^{2/3}}{\left(\frac{\chi}{1+\mu} \right) + \left(\frac{\kappa_c}{\kappa_{ref}} \right)^{2/3}} \right]^{\frac{3(\mu+1)}{2}} \tag{15}$$

where κ_{ref} is the wavenumber that refers to the large scales, $\kappa_{ref} = \epsilon/k^{3/2}$. With $\kappa_c = \pi/\Delta$, the f_k parameter in Eq.(15) may be reformulated as

$$f_k = \frac{k_u}{k} = 1 - \left[\frac{\left(\frac{\Lambda}{\Delta} \right)^{2/3}}{\frac{\chi}{(1+\mu)\pi^{2/3}} + \left(\frac{\Lambda}{\Delta} \right)^{2/3}} \right]^{\frac{3(\mu+1)}{2}} \tag{16}$$

For simplicity of the analysis, let μ = -1/3, which leads to $\frac{3(\mu+1)}{2} \rightarrow 1$. The ratio k_u/k in Eq.(16) becomes

$$f_k = \frac{k_u}{k} = \frac{1}{1 + \frac{2\pi^{2/3}}{3\chi} \left(\frac{\Lambda}{\Delta} \right)^{2/3}} \tag{17}$$

The value of the exponent μ will have a substantial effect on mainly large scales, i.e., when $\Lambda/\Delta \gg 1$. In the limiting case, $f_k = \frac{k_u}{k} \approx \frac{1}{\frac{2\pi^{2/3}}{3\chi}\left(\frac{\Lambda}{\Delta}\right)^{2/3}}$ which is exactly equal to what one gets when using Eq.(13) with the energy spectrum of the inertial range, i.e., $E(\kappa) = \chi\epsilon^{2/3}\kappa^{-5/3}$ resulting in the following formulation

$$f_k = \frac{k_u}{k} = \frac{\int_{\kappa_c}^{\infty} E(\kappa)d\kappa}{k} = \frac{1}{\frac{2\pi^{2/3}}{3\chi}\left(\frac{\Lambda}{\Delta}\right)^{2/3}} \tag{18}$$

This is similar to the one proposed by Girimaji and Abdol-Hamid (2005) using Kolmogorov length scale however, with a different constant, i.e., $f_k = k_u/k = 1/\sqrt{(C_\mu)(\Lambda/\Delta)^{2/3}}$. Figure 3 shows the f_k distributions of Eq.(16) for $\mu = -1/3$, $\mu = 2$, and $\mu = 4$, as well as Eq.(18) and the formulation used by Girimaji and Abdol-Hamid (2005). The latter is too dissipative and thus cannot resolve small scales. f_k with $\mu = -1/3$ on the other hand, is too restrictive and barely approaches one at low wave numbers. This in turn renders an imbalance in model's terms in near-wall regions where $\Lambda/\Delta \ll 1$. Both of the f_k formulations with $\mu = 2$, and $\mu = 4$ fall within an envelope of f_k based on $\mu = -1/3$ and $f_k = \frac{1}{\frac{2\pi^{\frac{2}{3}}}{3\chi}\left(\frac{\Lambda}{\Delta}\right)^{\frac{2}{3}}}$. The objective here is to transform f_k into f_{ν_t}, which is based on

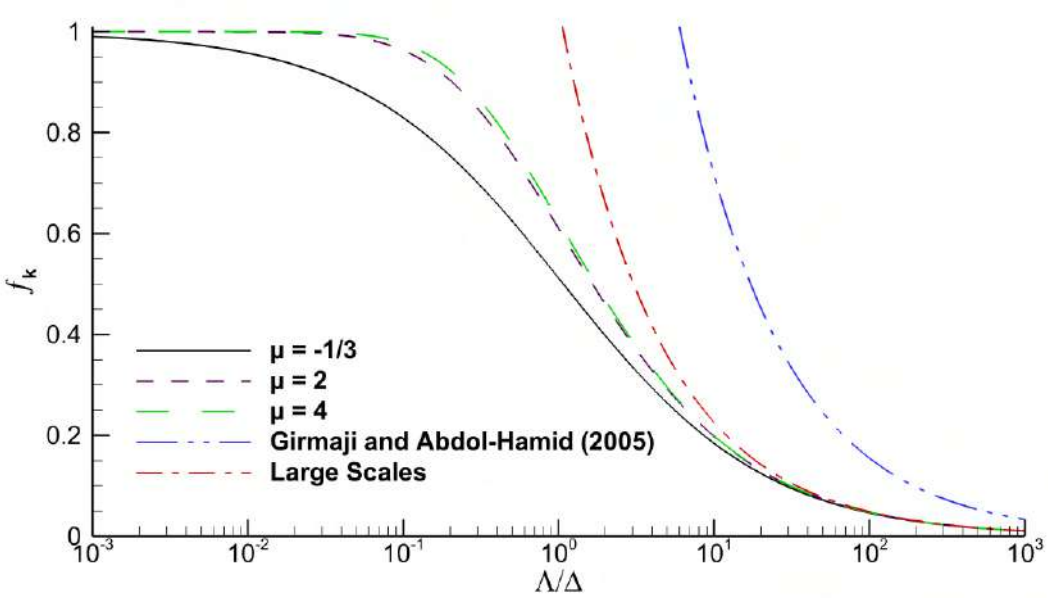

Figure 3: f_k distributions against the non-dimensional length scale Λ/Δ

the ratio of the unresolved to total turbulent viscosity ν_{tu}/ν_t. Although, Eq.(17)

will not be the selected parameter in the present model, it constitutes a good starting point for this transformation. In the unresolved/subgrid domain, the equilibrium hypothesis implies that $\nu_{tu}S^2 = C_E k_u^{3/2}/l_{sgs}$ and $\nu_{tu} = C_{sgs} l_{sgs} k_u^{1/2}$ combining both yields $\nu_{tu} = \sqrt{(C_E C_{sgs})} k_u / S$. When the upper limit is reached, $k_u \to k$ and $\sqrt{(C_E C_{sgs})} \to a$. following Bradshaw's hypothesis, $\nu_t = ak/S$ where $a = 0.3$ (Bradshaw et al., 1967). Therefore, Eq.(17) may be rewritten as

$$f_{\nu_t} = \frac{\nu_{tu}}{\nu_t} = \frac{k_u}{k} = \frac{1}{1 + \frac{2\pi^{2/3}}{3\chi a}\left(\frac{\nu_t/S}{\Delta^2}\right)^{1/3}} \tag{19}$$

Where the total kinetic energy and its dissipation rate follows from $k = \nu_t S/a$ and $\epsilon = \nu_t S^2$. Solving the f_k parameter analytically requires the knowledge of the total kinetic energy, or the resolved part of it. To overcome this obstacle, the $k - \epsilon$ model, utilizing the RANS approach, has to be solved or the total kinetic energy has to be computed based on the resolved part using $k_r = \sum_{i=1}^{3} \left(\overline{u_i} - u_i\right)^2$ and the unresolved one obtained from the model based on the previous time step. While the first approach requires the solution of a turbulence model, i.e., two extra differential equations, the second necessitates averaging over a long period of time. Both of these approaches require additional computational cost that could be averted if f_{ν_t} is a function of $\left(\frac{\nu_{tu}/S}{\Delta^2}\right)$. The choice of $\mu = -1/3$ renders the analytical solution of Eq.(19) to formulate $f\left(\frac{\nu_{tu}/S}{\Delta^2}\right)$ possible, and takes the following form

$$f_{\nu_t} = \frac{1}{1 + A + \frac{\beta\eta_{tu}^2}{3A}} \tag{20}$$

With

$$A = \left(\frac{\beta\eta_{tu}^2}{2} + \sqrt{\frac{\beta^2\eta_{tu}^4}{4} - \frac{\beta^3\eta_{tu}^6}{27}}\right)^{1/3} \tag{21}$$

$$\beta = \left(\frac{2\pi^{2/3}}{3\chi a}\right)^3 \tag{22}$$

$$\eta_{tu}^2 = \frac{\nu_{tu}/S}{\Delta^2} \tag{23}$$

It is worth to note that the Smagorinsky constant C_s may be expressed by $C_s^2 = \frac{\nu_{tu}/S}{\Delta^2}$, which is the variable non-dimensional length-scale ratio η_{tu}^2 in the present work. Hence, η_{tu} is a dynamically adjusting ratio depending on flow characteristics and grid size. The previous arguments may also be used to rewrite Eq.(18) in terms of f_{ν_t}, or

$$f_{\nu_t} = \frac{\nu_{tu}}{\nu_t} = \frac{1}{\frac{2\pi^{\frac{2}{3}}}{3\chi a}\left(\frac{\nu_t/S}{\Delta^2}\right)^{\frac{1}{3}}} \tag{24}$$

Which may also be formulated as $f_{\nu_t} = f(\nu_{tu}/\nu_t)$, i.e.,

$$f_{\nu_t} = \frac{1}{\left(\frac{2\pi^{\frac{2}{3}}}{3\chi a}\right)^{3/2} \eta_{tu}} \tag{25}$$

This equation follows from the inertial range, while Eq.(20) is expected to be very restrictive. One way to utilize Eq.(25) is to either use a damping function in near-wall regions when $\eta_{tu} \ll 1$, or to follow an analogous approach to that of Chaouat and Schiestel (2009) who proposed the following equation for k_u/k

$$f_k = \frac{k_u}{k} = \frac{1}{\left(1 + \left(\frac{2\pi^{2/3}}{3\chi}\right)^{9/2} \left(\frac{\Lambda}{\Delta}\right)^3\right)^{2/9}} \tag{26}$$

With a Kolmogorov constant $\chi = 1.3$ rather than 1.5 rendering Eq.(26) to work better when performing LES simulations on coarse grids that are typically encountered in practical engineering applications (Chaouat & Schiestel, 2009). By comparing Eq.(26) and Eq.(25), it becomes evident that one can formulate a new equation analogous to Eq.(26) that avoids a value of more than 1 when $\eta_{tu} \ll 1$ and retains the same behavior in the inertial range. f_{ν_t} maybe formulated as

$$f_{\nu_t} = \frac{\nu_{tu}}{\nu_t} = \frac{1}{\left(1 + \left(\frac{2\pi^{2/3}}{3\chi a}\right)^{27/4} \eta_{tu}^{9/2}\right)^{2/9}} \tag{27}$$

Figure 4 depicts the behavior of $f_{\nu_t} = \nu_{tu}/\nu_t$ using Eq.(20), Eq.(25), and Eq.(27). It is obvious that Eq.(27) is much closer to the one derived using the inertial range, i.e., Eq.(25) while bounding it to one in regions when $\eta_{tu} \ll 1$. Another

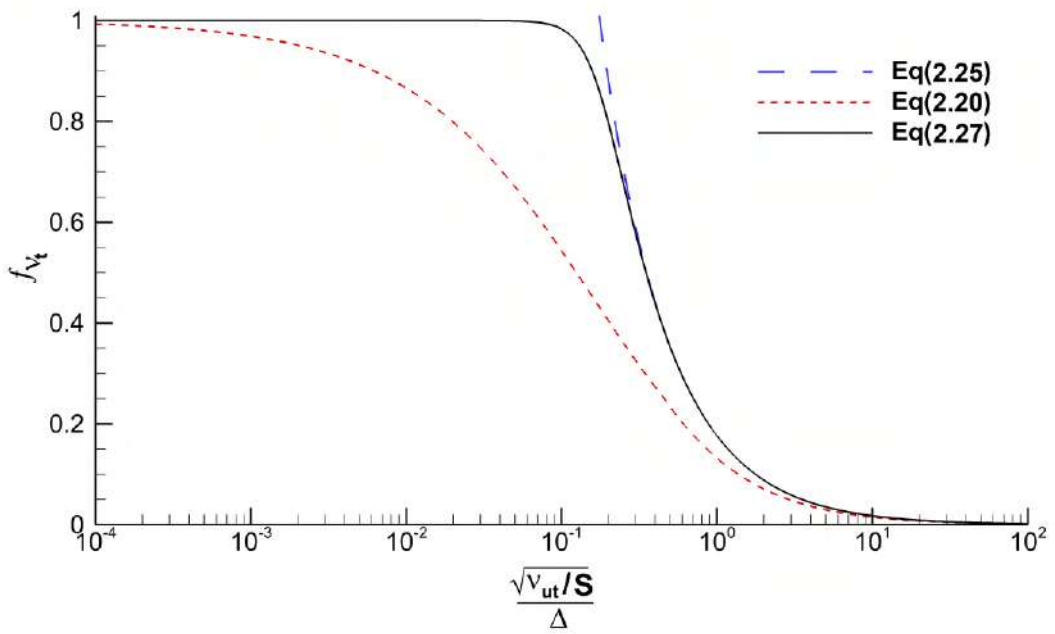

Figure 4: f_{ν_t} distributions against the non-dimensional length scale η_{tu}

approach inspired by the work of Fadai-Ghotbi et al. (2010) in which a wall function is used in conjunction with an f parameter based on the inertial range. In the present case, Eq.(25) is used to formulate a new f_{ν_t} that goes to unity as the wall is approached. Consider the following

$$f_{\nu_t} = min\left[1, (1 - D^p) + \frac{D^p}{\left(\frac{2\pi^{2/3}}{3\chi a}\right)^{3/2} \eta_{tu}}\right] \tag{28}$$

where D is a damping function that yields $f_{\nu_t} = 1$ in the near wall vicinity. The correct wall-limiting behavior is $D^p \propto y^p$ with the asymptotic wall behavior $\frac{dU}{dy} \propto y^0$ and the undamped eddy viscosity $\nu_{tu} \propto y$. In the near-wall vicinity, it may be assumed that $\Delta \propto y^n$. Therefore, $\eta_{tu} \propto y^{1/2-n}$ and the last term in

Eq.(28) should be

$$0 < \left((1 - D^p) + \frac{D^p}{\left(\frac{2\pi^{2/3}}{3\chi a}\right)^{3/2} \eta_{tu}} \right) \ll 1 \tag{29}$$

and thus the power of each term should be greater than zero. For $(1 - D^p)$, $p > 0$ and for the last term, $\frac{D^p}{\left(\frac{2\pi^{2/3}}{3\chi a}\right)^{3/2} \eta_{tu}}$, one can write $p - \left(\frac{1}{2} - n\right) > 0$ or $p > \left(\frac{1}{2} - n\right)$. Now a grid length scale based on the following equation could be assumed $\Delta = [\Delta_x \Delta_y \Delta_z]^{1/3}$ and with near wall clustering, it could be assumed that $\Delta_x \sim 1$, $\Delta_y \sim y$, and $\Delta_z \sim 1$ yields $n = 1/3$. Therefore, $p > 1/6$. Now, considering the current damping function that is used in the model

$$D_2 = 1 - e^{-\left(\frac{\nu_{tu}}{\nu\kappa A}\right)^2} \tag{30}$$

The first term of the series expansion of Eq.(30) is $D_2 \sim \left(\frac{\nu_{tu}}{\nu\kappa A}\right)^2 + ...$, or $D_2 \sim y^2 + ...$, thus, $p = 2$ according to the existing damping function. $\sqrt{D_2}$ satisfies the required coefficient yielding $p = 1$. Therefore, the final form could be

$$f_{\nu_t} = min \left[1, \left(1 - \sqrt{D_2}\right) + \frac{\sqrt{D_2}}{\left(\frac{2\pi^{2/3}}{3\chi a}\right)^{3/2} \eta_{tu}} \right] \tag{31}$$

2.3 Relationship to the Smagorinsky model

To shed light on the connection between the present model and that of Smagorinsky (1963), consider the case when, $\frac{\nu_t/S}{\Delta^2} \gg 1$. f_{ν_t} reduces to $\frac{1}{\beta^{1/2}\eta_{tu}}$. Furthermore, it is easy to deduce from Eq.(18) that

$$\epsilon = \frac{\pi}{\Delta} \left(\frac{2}{3\chi}\right)^{3/2} k_u^{3/2} \tag{32}$$

Using the subgrid equilibrium for the current turbulence model, i.e., $\nu_{tu} S c_1 = c_2 \nu_{tu}^2 / (f_{\nu_t} L_{vk}^2)$ and $a k_s = \nu_{tu} S$, the term k_u can be eliminated from Eq.(32) resulting in

$$\epsilon = \frac{\pi}{\Delta} \left(\frac{c_2}{c_1} \right)^{3/2} \left(\frac{2}{3a\chi} \right)^{3/2} \left(\frac{\nu_{tu}^2}{f_{\nu_t} L_{vk}^2} \right)^{3/2} \tag{33}$$

Eliminating $\nu_{tu} = (c_1/c_2) S f_{\nu_t} L_{vk}^2$ and noting that $\epsilon = (C_s \Delta)^2 S^3$ we can solve for C_s Eq.(33) can be rearranged as

$$C_s^2 = \frac{\pi}{\Delta^3} \left(\frac{c_1}{c_2} \right)^{3/2} \left(\frac{2}{3a\chi} \right)^{3/2} \left(f_{\nu_t} L_{vk}^2 \right)^{3/2} \tag{34}$$

When $f_{\nu_t} \rightarrow \frac{1}{\beta^{1/2} \eta_{tu}}$, $\beta^{1/2} \eta_{tu} > 1$ or $\Delta^2 / \beta < \nu_{tu} / S$. Eliminating ν_{tu}/S by using the subgrid equilibrium, $\nu_{tu}/S = (c_1/c_2) L_{vk}^2 f_{\nu_t}$, it is easily deduced that $(\Delta^2/\beta)(c_2/c_1) < L_{vk}^2 f_{\nu_t}$. Therefore, Eq.(34) may be written as

$$C_s > \frac{\left(\frac{3}{2} \chi a \right)^{3/2}}{\pi} \tag{35}$$

With Kolmogorov constant of 1.5 and $a = 0.31$, $C_s = 0.1765$ which falls is very close to the theoretical value of 0.18 found by Lilly (1967) and within the widely accepted range of 0.1-0.2

Chapter Three

Numerical Method

3.1 Numerical Considerations

The partially averaged method has been around for some time with extensive validation performed for the various formulations based on RANS models. As was pointed out in the previous chapters, the vast majority of these models use two equations for closure, one for the unresolved turbulent kinetic energy k_u and the other is usually either for the unresolved dissipation rate ϵ_u or the unresolved specific dissipation rate ω_u. However, since the proposed model rely on one equation for the unresolved turbulent viscosity, further investigation is needed. In order to validate the use of the proposed model, two experimental test cases are considered in this study, i.e., the backward-facing step and the external flow over a simplified car. More detailed description and numerical setup of both cases are presented in the next sections. In addition to experimental data, comparison is carried out against the Improved Delayed Detached Eddy Simulation (IDDES) based on the $k-\omega$ SST model, and Wall Modeled Large Eddy Simulation (WMLES). The reason behind these choices is that the latter represents the class of models where only modeling is performed at the wall level, while the former completely shields the boundary layer. The proposed model is able -if given the adequate mesh resolution- to seamlessly switch from modelling to resolving without the abrupt switch between the two formulations. It is expected that using PANS will provide an intermediate level of modelling between the two approaches. To perform the numerical simulations, the commercial finite volume solver, ANSYS Fluent 2019R3 is used. All computations are carried out using double precision to ensure round-off errors have insignificant effect on the solution. Since only

incompressible cases are considered in this study, the pressure-based solver is chosen, with the pressure-velocity formulation set to coupled. The momentum equations are solved using the bounded 2nd order central scheme as recommended by the Scale-Resolving best practices guidelines (Menter, 2012), while the turbulence equations for IDDES (k and ω) and the transport equation for the newly proposed scalar are solved using 2nd order upwind schemes. Pressure is computed with second order accuracy. The temporal discretization is set to implicit 2nd order and the time step is chosen per case, as to satisfy a Courant-Friedrichs-Lewy (CFL) number smaller than unity in over 99% of the domain. Since the proposed model is closed by solving the transport equation of the unresolved turbulent viscosity ν_{tu}, a user-defined function (UDF) is developed and compiled in Fluent. This UDF has two main functions; the first is to define the different terms of the transport equation (production, dissipation, transport, etc.) and the second is to assign the solution of the equation to the turbulent viscosity in the momentum equation after applying some damping using Eq.(30). An overview of the UDF is given in the following section. The computations of this study are performed on a cluster of 7 nodes with a total of 112 cores (Intel Xeon CPU E5-2650 v3 @2.3GHz). The computational resources as well as the ANSYS Fluent licenses were provided by the School of Engineering at the Lebanese American University.

3.2 User Defined Function (UDF)

In order to use the proposed model in the numerical simulations, the scalar transport equation of the unresolved turbulent viscosity ν_{tu} should be solved along with the momentum equations. The solver used in this study i.e., ANSYS Fluent, allows the addition of such equations when complied as User Defined Functions (UDFs). This requires transforming the derived mathematical model in the previous chapter, to a machine code. In this section, an overview of the UDF code is shown with emphasis on its most important parts. First, it should

be noted that although the code is written in the C language (as required by the solver), some predefined macros are used to define the different terms of the transport equation, and to read/write the flow variables calculated by the solver. The first section is the DEFINE_UDS_UNSTEADY macro, which is used to discretize the unsteady term $\frac{\partial \nu_{tu}}{\partial t}$ in the transport equation. Fluent normally treats such terms using the following equation written for the scalar variable Φ, equivalent to ν_{tu} in the current study (*ANSYS Fluent Customization Manual*, 2019)

$$unsteady\ term = -\int \frac{\partial}{\partial t}(\rho\Phi)dV = -\left[\frac{(\rho\Phi)^n - (\rho\Phi)^{n-1}}{\Delta t}\right]\Delta V = apu * \Phi^n + su \tag{36}$$

With $apu = -\frac{\rho\Delta V}{\Delta t}$ and $su = -\frac{\rho\Delta V}{\Delta t}\Phi^{n-1}$ In the current study the values of apu and su are changed to the following formulations

$$apu = -\frac{2}{3}\frac{\rho\Delta V}{\Delta t} \tag{37}$$

$$su = -\frac{V}{\Delta t}\left(2\rho\Phi^{n-1} - \frac{1}{2}\rho^{n-2}\Phi^{n-2}\right) \tag{38}$$

The convection term $U_j\frac{\partial \nu_{tu}}{\partial x_j}$ is then tackled under the DEFINE_UDS_FLUX macro. In this study, the unresolved turbulent viscosity is convected by the instantaneous velocity field U_j, thus no special treatment is required for this term, as U_j is the default flux used for User Defined Scalar (UDS). To model the transport term $\frac{\partial}{\partial x_j}\left(\left(\nu + \frac{\nu_{tu}}{\sigma}\right)\frac{\partial \nu_{tu}}{\partial x_j}\right)$, the diffusion coefficient is specified in the DEFINE_DIFFUSIVITY macro. The term $\nu + \frac{\nu_{tu}}{\sigma}$ is returned as the diffusion coefficient. The remaining terms in the transport equation are the source term $D_1 c_1 S\nu_{tu}$ and sink (or destruction) term $-\frac{c_2}{f_{\nu_t}}\frac{\nu_{tu}^2}{L_{vk}^2}$. In ANSYS Fluent both terms are specified under one macro, i.e., DEFINE_SOURCE. The combination of the source and sink terms is second order in the main variable ν_{tu}, so directly supplying the gradient of those terms reduces the order of the equation back to linear, increasing the matrix dominance. The final form of the returned source/sink term

and their derivatives are

$$D_1 c_1 S \nu_{tu} - \frac{c_2}{f_{\nu_t}} \frac{\nu_{tu}^2}{L_{vk}^2} \tag{39}$$

$$D_1 c_1 S - 2 \frac{c_2}{f_{\nu_t}} \frac{\nu_{tu}}{L_{vk}^2} \tag{40}$$

With the different terms of the transport equation accounted for, a solution for the unresolved turbulent viscosity ν_{tu} is now possible. To derive the correct turbulent viscosity the DEFINE_TURBULENT_VISCOSITY is used. Damping is applied on the unresolved viscosity using

$$\nu_{turb} = \nu_{tu} \left(1 - exp \left(\frac{\nu_{tu}/\nu}{A\kappa} \right)^2 \right) \tag{41}$$

With $A = 12$ and $\kappa = 0.41$.

The DEFINE_ADJUST is finally used to update the solution of the unresolved turbulent viscosity and assign the gradient values.

3.3 Wall Modeled Large Eddy Simulation

The Wall Modeled Large Eddy Simulation (WMLES) proposed by Shur et al. (Shur et al., 2008) is a hybrid model directly aimed at reducing the dependence of the LES grid requirements on the Reynolds' number. The motivation behind WMLES is to model only the innermost part of the boundary layer where the turbulent scales are the smallest and most expensive to resolve. The outer part of the boundary layer as well as the free-shear regions are solved using a regular LES formulation. The wall-normal grid resolution in the inner layer (near the wall) is comparable to RANS with a $y^+ < 1$ and similar to a resolved LES in the outer portion. On the other hand, the streamwise and spanwise grid requirements only scale with the boundary layer thickness, thereby exponentially reducing the total number of elements needed compared to a resolved LES as the Reynolds' number is increased. It was shown that WMLES is able to accurately predict velocity and

turbulent stress profiles in a periodic channel flow case with a Reynolds number based on the channel half-width Re_H varying from 395 to 18,000 (Menter, 2012). The interesting point there is that same grid was used for all values of Re_H, with only couple of layers added along the wall normal direction to preserve the $y^+ < 1$ requirement. The number of elements used in both the streamwise and spanwise was not changed, simply because the boundary layer thickness is specified by the geometry of the channel i.e., the channel half-width H which is constant. This proves that WMLES can be used instead of a fully resolved LES in boundary layers flows.

The WMLES model used in the current study is the default formulation adopted by ANSYS Fluent (*ANSYS Fluent Theory Guide*, 2019). The solver only accounts for an algebraic equation for the subgrid viscosity defined as

$$\nu_{sgs} = min\{(\kappa y)^2, (C_{SMAG}\Delta)^2\}\{1 - exp\left[-(y^+/25)^3\right]\}S \tag{42}$$

The first term of the above formulation combines the Prandtl's mixing length model i.e., $(\kappa y)^2$ and the Smagorinsky subgrid model i.e., $(C_{SMAG}\Delta)^2$. The second term is the damping function proposed by Piomelli et al. (Piomelli et al., 1988).

The subgrid length scale used in the above equation is computed using

$$\Delta = min\{max[C_w d_w, C_w h_{max}, h_{wn}], h_{max}\} \tag{43}$$

Where h_{wn} is the grid size in the wall normal direction and C_w an empirical constant set to 0.15. For the detailed derivation and formalism of WMLES the reader is referred to the original paper (Shur et al., 2008).

3.4 Improved Delayed Detached Eddy Simulation

The formulation of the Improved Delayed Detached Eddy Simulation (IDDES) is presented below. The IDDES was developed as an improvement for the DDES, which in turn is an improved version of the original DES model proposed by Spalart et al. (1997). As mentioned in the first chapter, the DES is a zonal hybrid RANS/LES model that shields the boundary layer from any resolved content and uses LES elsewhere i.e., in the free shear regions away from walls. This zonal behavior is enforced by using a modified length scale in the destruction term of the turbulent kinetic energy equation that takes the following form

$$\frac{\partial k}{\partial t} + \overline{U}_j \frac{\partial k}{\partial x_j} = P_k + \frac{\partial}{\partial x_j}\left(\left(\nu + \frac{\nu_t}{\sigma_k}\right)\frac{\partial k}{\partial x_j}\right) - \frac{k^{3/2}}{min(L_t, C_{DES}\Delta_{max})} \tag{44}$$

With $\Delta_{max} = max(\Delta_x, \Delta_y, \Delta_z)$ and $L_t = \frac{k^{3/2}}{\epsilon} = \frac{\sqrt{k}}{\beta^*\omega}$. It should be noted that Eq.(44) assumes incompressible flow and is only valid for models in which the turbulent kinetic energy is a solved quantity. For DES based on other families of RANS models, like for example, the 1-equation of Spalart-Allmaras, the same treatment is applied to the destruction term of the modified turbulent viscosity $\tilde{\nu_t}$.

When $C_{DES}\Delta_{max} > L_t$, the model goes to the original RANS formulation, and when $C_{DES}\Delta_{max} < L_t$ an LES form is recovered based on $C_{DES} = 0.65$. Without going into unnecessary details about the underlying principles of DES, it should be pointed out that if Δ_{max} gets small enough, LES equations would be used inside the boundary layer. However, if Δ_{max} is not small enough to satisfy LES requirements, an ambiguous solution is recovered. This represents one of the biggest weaknesses of DES often referred to as Grid Induced Separation (GIS). To circumvent the GIS, stronger shielding was applied to the boundary layer via the length scale used in the turbulent kinetic energy destruction term with the

Delayed DES (DDES) (P. R. Spalart et al., 2006) using

$$l_{DDES} = L_t + f_d max(0, L_t - C_{DES}\Delta_{max}) \tag{45}$$

Where l_{DDES} is the new length scale, and f_d the new shielding function defined as

$$f_d = 1 - tanh\left[(C_{d1}r_d)^{C_{d2}}\right] \tag{46}$$

With $C_{d1} = 8$, $C_{d2} = 3$ and

$$r_d = \frac{\nu + \nu_t}{\kappa^2 d_w^2 \sqrt{0.5(S^2 + \Omega^2)}} \tag{47}$$

Where d_w is the distance to the closest wall, S is the mean strain rate, and Ω is the mean vorticity rate. In IDDES further improvement is made where the model is able to recover the WMLES formulation of the previous section when enough turbulent content is available. Otherwise, the model switches back to the a regular DDES formulation (Shur et al., 2008).

Details of the DES, DDES, and IDDES can be found in the original papers of Spalart et al. (1997), Spalart et al. (2006), and Shur et al. (2008)

Chapter Four

Cases Setup

4.1 Backward-Facing Step

The backward-facing step is considered to be an interesting, yet challenging test case among the turbulence modelling community. Its popularity does not only stem from the simplicity of the geometry and abundance of experimental data, but also from the several flow mechanics involved, i.e., flow separation, vortex shedding and pairing of the vortices. Several experimental studies were conducted to tackle this phenomenon, of which, the works of Driver and Seegmiller (1985) will serve as the primary reference for the current study. The computational domain adopted in the current study is portrayed in Figure 5. The step height H is equal to $0.0127m$, the same value used in the experiments. The domain is composed of an inlet section with dimensions $4H$ x $8H$ x $4H$ ($0.0508m$ x $0.1016m$ x $0.0508m$) upstream of the step and a downstream section with dimensions $50H$ x $9H$ x $4H$ ($0.635m$ x $0.1143m$ x $0.0508m$). The resulting expansion ratio (ratio of the downstream-to-upstream height) is 1.125 for which the pressure gradient due to the sudden expansion has negligible effect on the turbulent transport (Badri Narayanan et al., 1974). The density ρ is set to 1.1962 kg/m^3 and dynamic viscosity ν to $1.7894e^{-5}$ $Pa.s$. The Reynolds' numbers based on the step height H is set to $37,500$ with an inlet Mach number of 0.128 replicating the experimental conditions. To ensure appropriate flow conditions are provided at the inlet, a precursor channel flow case is performed. Velocity components and turbulent quantities are extracted, then imposed at the inlet of the domain at a distance of $4H$ upstream of the step. The time-step is set to $5 * 10^{-6}$ seconds in all runs to maintain a maximum Courant–Friedrichs-Lewy (CFL) number of 1.

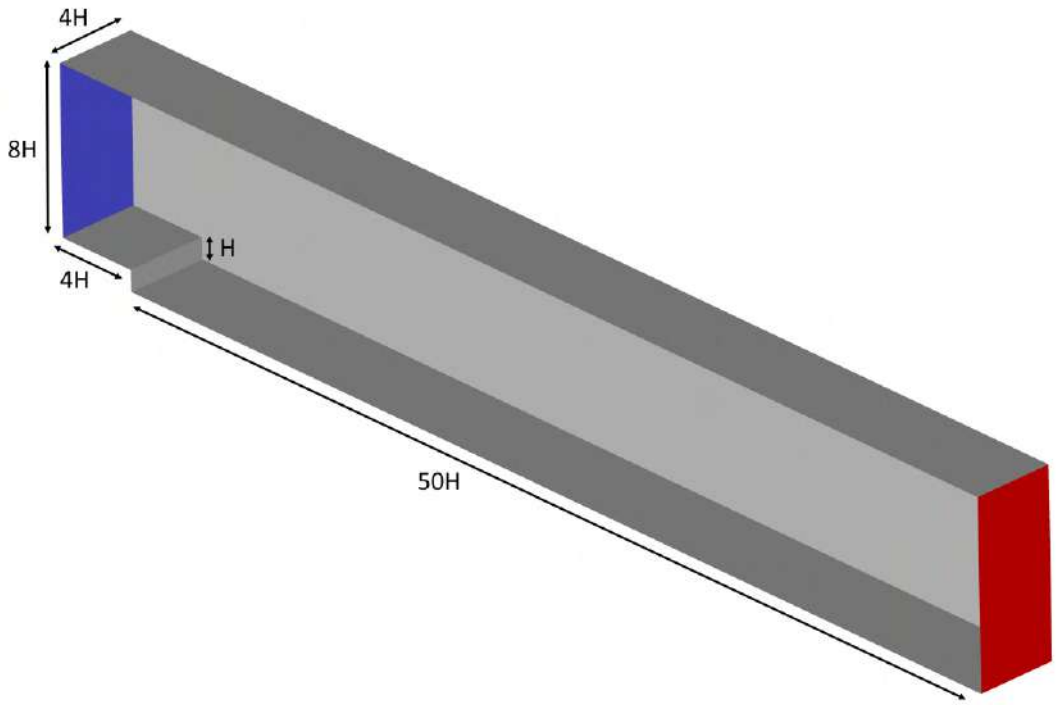

Figure 5: Backward-facing step computational domain geometry

Three mesh densities of 1, 5, and 20 million elements are investigated and will be referred to as coarse, medium, and fine subsequently. Details of the mesh densities are reported in Table 1 and cross-sections of the grids are presented in Figure 6. All cases are initialized from steady state RANS solutions and allowed to run long enough to pass the transient phase i.e., at least 200 flow-through the step (1 flow-through being equivalent to the time needed for the flow to cover a distance of 1 step height H in this case). Sampling of the solution is then performed for a total time of 0.75 seconds or what is equivalent to over 2500 flow-through the step. The results are presented in the next Chapter.

Table 1: Grid distributions for the 3 meshes of the backward-facing step

Elements	Mesh 1 (Coarse)	Mesh 2 (Medium)	Mesh 3 (Fine)
Upstream 4H	10	10	10
Downstream 50H	250	450	850
Step H	50	100	150
Vertical 8H	50	100	150
Spanwise 4H	40	60	80
Total	1,020,000	5,460,000	20,520,000

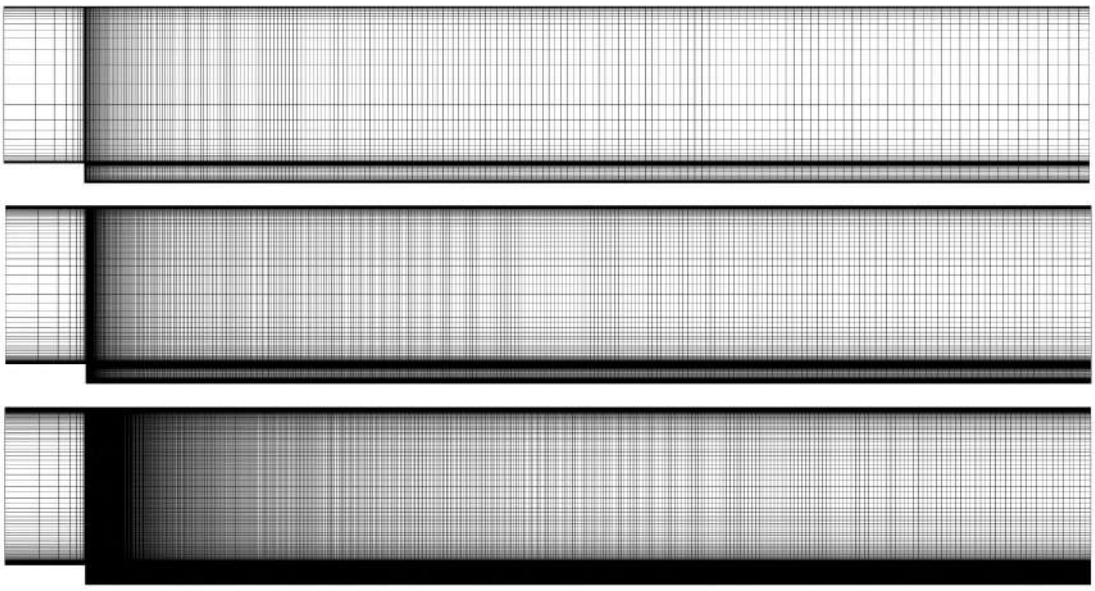

Figure 6: Grids of the backward-facing step. From top to bottom: Coarse, Medium, and Fine mesh

4.2 Ahmed Body

The second test case considered in this study is the flow over a simplified car model, proposed by Ahmed et.al. (1984), thus it will be referred to as the Ahmed body subsequently. Despite being a simplified version of a car, this test case remains quite challenging because it exhibits the common flow features of a real vehicle i.e., flow separation and reattachment. The reference sketches for the geometry are shown in Figure 7 with the appropriate dimensions. The

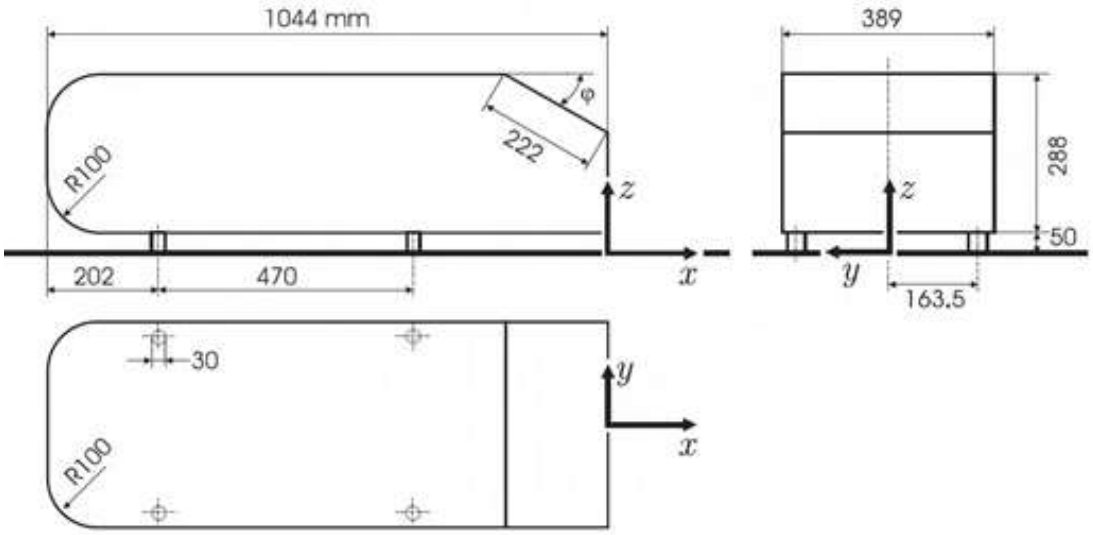

Figure 7: Reference sketches of the Ahmed body

Ahmed body has a length $L = 1044mm$, height $H = 288mm$, and a width $W = 389mm$. Ahmed et.al. (1984) have studied the separation over the slant and found that $\phi_c = 30^o$ is a critical slant angle. For larger angles ($\phi_c > 30^o$) the flow fully separates over the slant due to the strong adverse pressure gradient between the roof and slant. On the other hand, for angles smaller than the critical angle ($\phi_c > 30^o$), the flow reattaches over the slant. To show the fidelity of the proposed model in predicting reattachment behavior, as well as the velocity and turbulent stress profiles, a subcritical slant angle is selected i.e., $\phi_c = 25^o$. The computational domain has dimensions of $10L$ x $10H$ x $10W$ along the streamwise, normal, and spanwise directions respectively. The current domain dimensions are larger than the recommended design of the ERCOFACT guildines, to ensure it has no effect on the solution. The inlet is placed at $2L$ upstream of the body and outlet at $7L$ downstream. The body rests above the ground on 4 cylindrical legs of diameter $30mm$ and length of $50mm$ positioned as shown in Figure 7. The only defining parameter left is the Reynolds' number based on the body's height $Re_H = U_\infty H/\nu$, where U_∞ is the freestream velocity, H is the height of the body, and ν the kinematic viscosity of the fluid. To replicate the experimental conditions the inlet velocity is set to $40m/s$ resulting in $Re_H = 768,000$. The computational grid is generated in ANSYS Meshing with the patch conforming

tetrahedral algorithm that fully meshes the domain with unstructured tetrahedral cells and prism elements if inflation layers are present. The boundary layer is captured using 46 prism layers with the first layer having a thickness of $5 * 10^{-5}$ meters to keep y^+ below 1. The domain is divided into 4 regions with decreasing element size clustering the grid towards the body. The meshing parameters at the wall are taken from the mesh independent set-up of Wang (2019). The resulting grid is composed of 22 million elements and shown in Figures 8 and 9. The

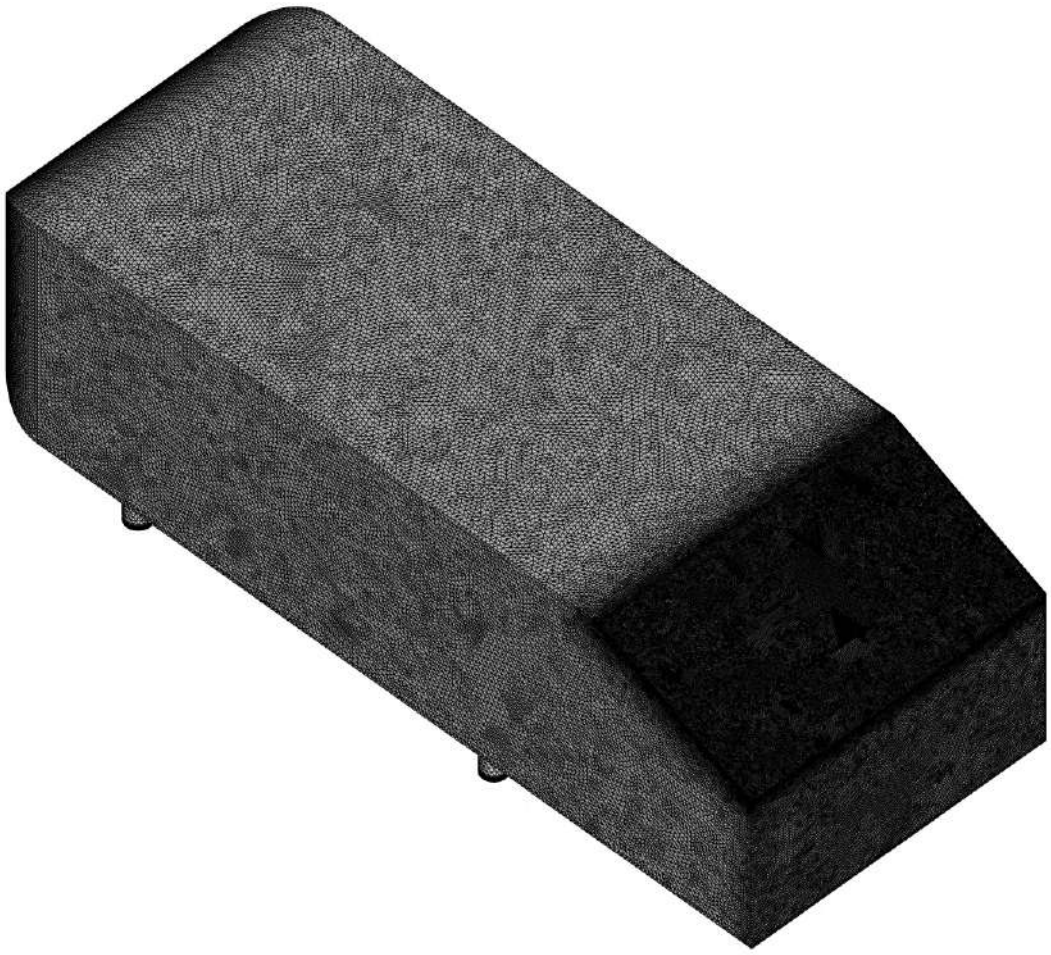

Figure 8: Mesh around the Ahmed body

solution is initialized with a steady RANS $k-\omega$ SST to save computing time when starting the unsteady mode. The simulations are first run for $20,000$ time-steps ($0.2s$) corresponding to around 8 flow-through for the length of the body, enough to cover the transient effects. To optimize the sampling process, the results are extracted at different stages i.e., $0.06s$, $0.12s$, $0.2s$, and $0.24s$ corresponding to 3,

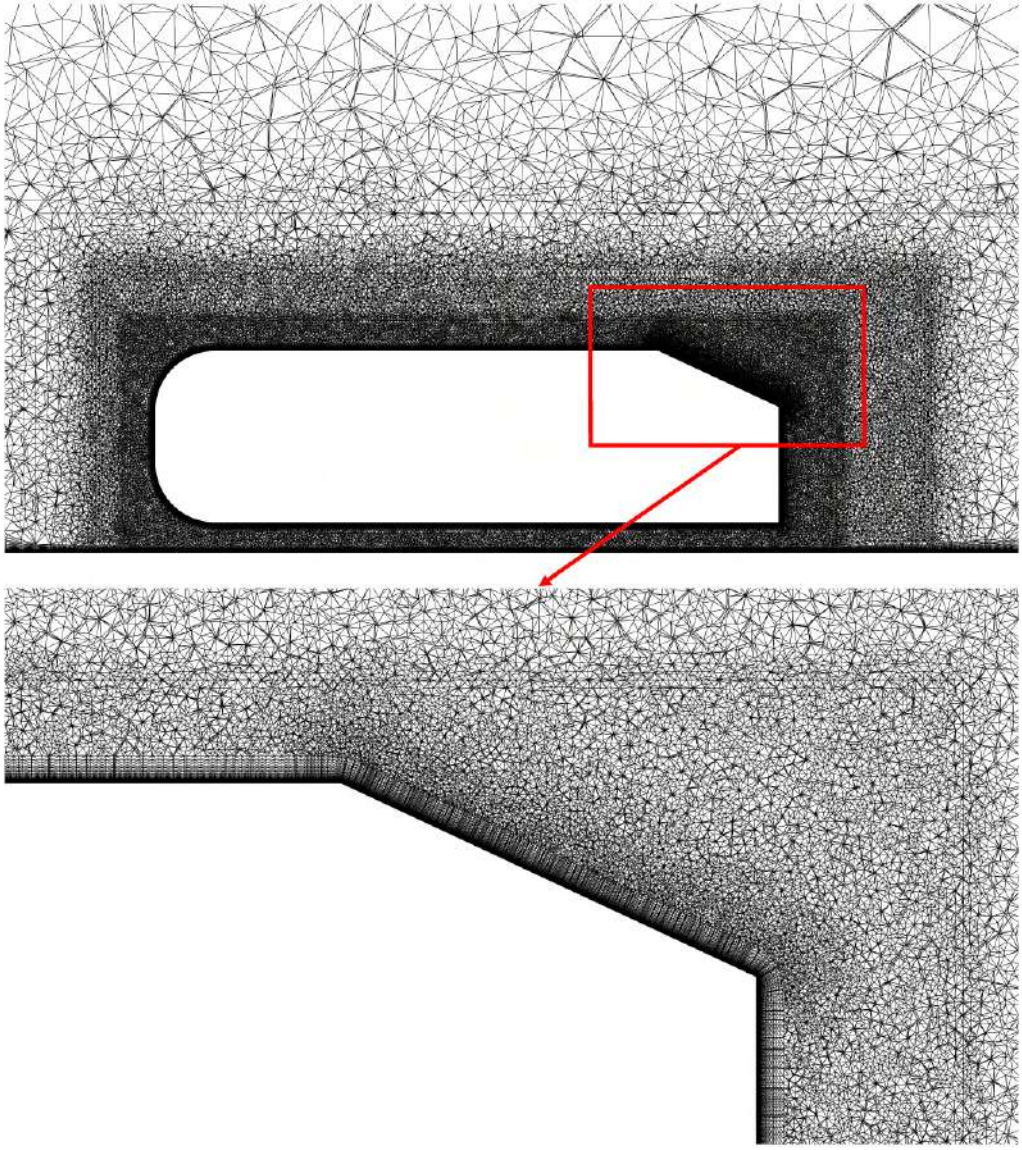

Figure 9: Mesh around the Ahmed body zoomed in on the slant

6, 8, and 10 flow through the Ahmed body. Results of the Ahmed body case are presented in the following Chapter.

Chapter Five

Results and Discussion

The results of the numerical calculations are presented in this Chapter as follows. Starting with the backward-facing step, the effect of the sampling time is first investigated. This is to determine the minimum sampling time needed for the convergence of averaged quantities. A mesh study is then carried out on the three levels of resolutions defined by the grid densities i.e., coarse, medium, and fine. Validation is then performed for the PANS model against the experimental data of Driver and Seegmiller (1985) along with the results of the IDDES and WMLES. The results of the Ahmed Body case are then presented. In the same spirit as the previous case, sampling time study is also performed since the geometry and physics are very different from the backward-facing step. Since only one mesh density is considered for this case, comparison will be directly carried out between PANS, IDDES, WMLES, and validation performed against the experimental data of Ahmed et. al. (1984), and the works of Lienhart et al. (2002).

5.1 Backward-Facing Step

5.1.1 Sampling Time

In order to draw meaningful conclusions out of the presented data, the effect of the sampling time on the averaged solution variables is first investigated. This time dependency study is specifically performed on PANS being the proposed model. Out of the three grids, the fine mesh is selected as it is the most computationally demanding one. The solution variables of interest are extracted at different times i.e., $0.05s$, $0.1s$, $0.2s$, $0.5s$, and $0.75s$, equivalent to 150, 300,

600, 1500, and 2500 flow-through the step. The mean skin friction coefficient c_f distributions against the streamwise distance normalized by the step height x/H are shown in Figure 10 at the different sampling times. It can be clearly seen that c_f barely changes form $0.5s$ to $0.75s$ indicating that $0.5s$ is enough. It is also interesting to note that at $0.2s$, c_f is almost converged expect a small region prior to reattachment. The reattachment length normalized by the step height X_r/H is reported in Table 2 for the different sampling times. From $0.2s$ to $0.5s$ X_r/H only changes by 0.5% while averaging for $0.75s$ further reduces the difference by 0.06% compared to $0.5s$. This behavior is similar to the one observed for the mean skin friction coefficient. This is because the reattachment length is equivalent to the location where c_f is zero (second intersection with x-axis). It is thus expected that the sampling requirements for the reattachment length should be similar to the mean skin friction coefficient, at least in the region around reattachment. Although averaged wall statistics seem to have stabilized at $0.2s$, it is also important to check the convergence of averaged flow variables. Profiles of mean streamwise velocity normalized by the free stream velocity U/U_{ref}, as well as the normalized turbulent shear stresses $u'v'/U_{ref}^2$ are extracted at several times during the simulation and shown in Figure 11 at the location $x = 1H$ and in Figure 12 at $x = 10H$ against the wall-normal distance normalized by the step height y/H. The first location ($x = 1H$) shows the convergence of the solution in the separation region while the second one ($x = 10H$) represents the region downstream reattachment. As shown in Figure 11 both velocity and turbulent stresses barely change after $0.2s$ in the separation region, while at least $0.5s$ are needed in the region after reattachment as can be seen in Figure 12. This difference could be attributed to the size of turbulent length and time scales which are smaller (higher frequencies/eddy wavenumber) in the separation region and larger (lower frequencies/eddy wavenumber) after reattachment. These scales are better shown in the Q-criterion contours which will be presented in the following sections. Overall, the averaged statistics at $0.5s$ seems to have stabilized for

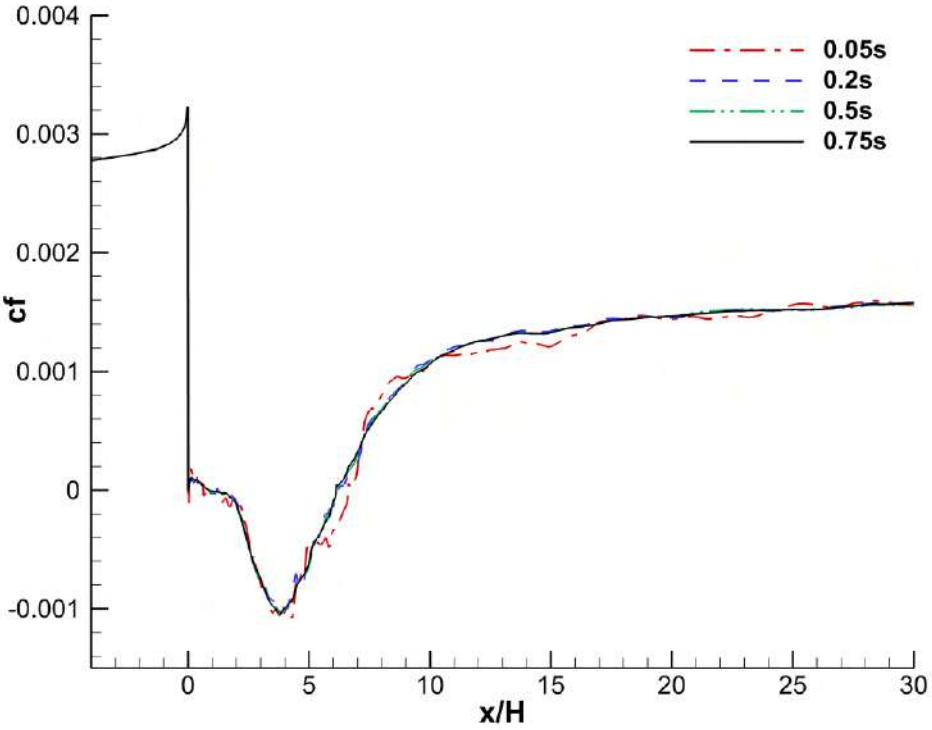

Figure 10: Convergence of mean skin friction coefficient for the PANS fine case

Table 2: Convergence of reattachment length for the PANS fine case

Sampled Time (s)	Reattachment Length X_r/H	% Change
0.05	6.64	-
0.1	6.54	-1.51%
0.2	6.28	-3.98%
0.5	6.27	-0.16%
0.75	6.27	0.00%

all variables (with some variables converging at half that value), thus, all the results of the backward-facing step in this study are extracted at $0.5s$ of each simulation. It is safe to assume that cases running on coarser grids should have larger modeled RANS portions which require less, or at the most, equal sampling times.

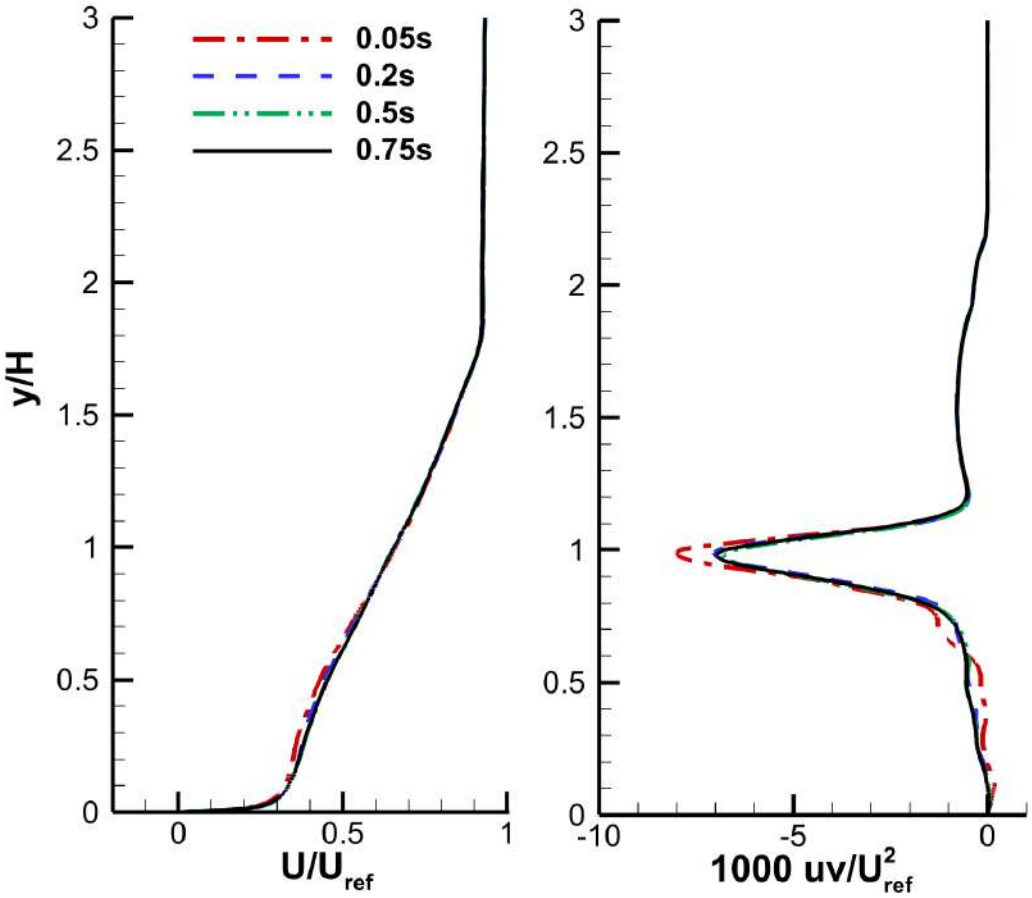

Figure 11: Convergence of velocity and turbulent shear stresses for the PANS fine case at x = 1H

5.1.2 Mesh study and model validation

The effect of mesh refinement on the solution and averaged flow variables is presented for the three models investigated. The mean skin friction coefficient c_f distributions on the bottom wall against the normalized streamwise distance x/H are plotted in Figure 13 for the coarse, medium, and fine meshes of the PANS runs. Figure 13 also includes the experimental data for a more insightful comparison. It can be seen that PANS performs well in the separation region for the three levels of resolutions, with the finest grid having the closest agreement with the experiment. However, downstream reattachment ($x/H > 8$) the solution of the coarse mesh is superior to the medium and fine meshes which roughly predicts the same distributions. The c_f distributions of IDDES shown in Figure

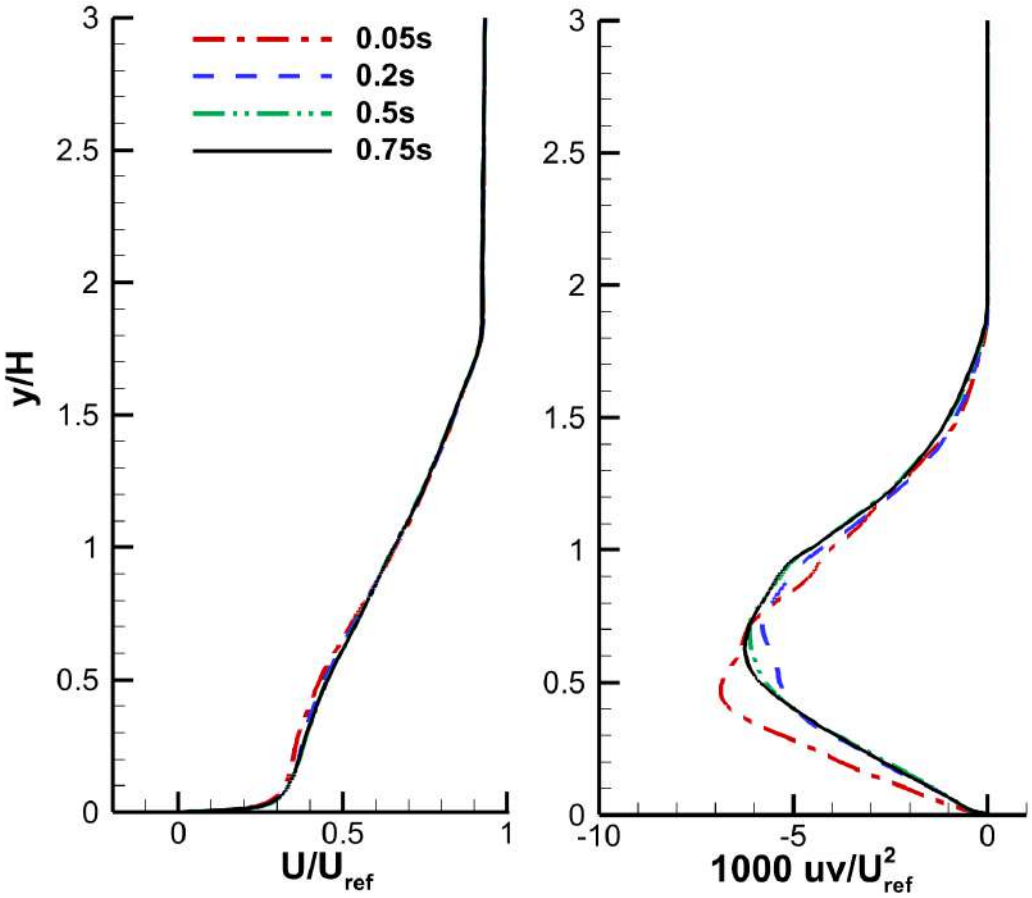

Figure 12: Convergence of velocity and turbulent shear stresses for the PANS fine case at x = 10H

14 have similar behavior to the ones predicted by PANS with good predictions in the separation region and decreasing trend after reattachment with the mesh density. On the other hand, WMLES completely misses the c_f in the separation region for the coarse mesh, but recovers the experimental solution in the far downstream i.e., $x > 16H$ as seen in Figure 15. Accuracy of the WMLES increases in the separation region with increasing mesh density with the finest mesh showing very good agreement with the experiments. Similar to PANS and IDDES, mesh refinement in the WMLES seems to result in lower c_f predictions after reattachment.

Reattachment lengths normalized by the step height X_R/H for the various models are reported in Table 3 or can be directly extracted from Figures 13, 14, and 15 where the skin friction coefficient is zero (second intersection with the x-axis).

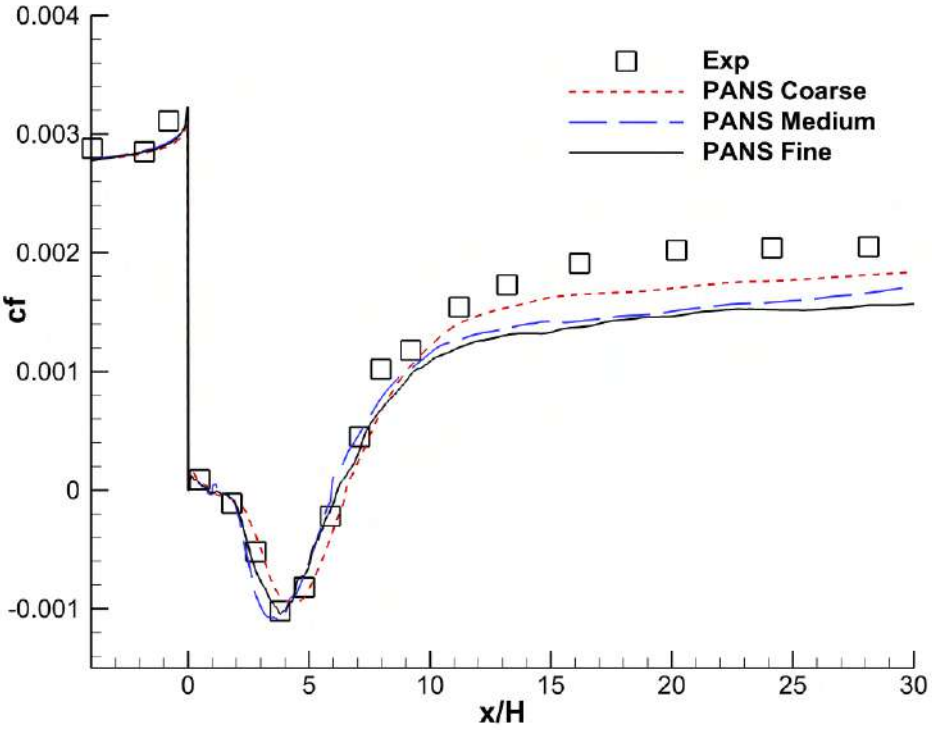

Figure 13: Mean skin friction coefficient distributions of PANS

X_R/H, as expected, shows similar behavior to the mean skin friction coefficient. As seen in Figure 16, WMLES shows continuous improvement with mesh refinement, while PANS and IDDES are relatively less sensitive to grid resolution and are within the experimental margin of error for the fines meshes.

Table 3: Reattachment Length X_R/H

Exp = 6.26 ± 0.1	WMLES	IDDES	PANS
Coarse Mesh	9.35	6.20	6.52
Medium Mesh	6.96	6.55	6.12
Fine Mesh	6.49	6.16	6.27

The mean skin friction coefficient c_f distributions on the bottom wall for the various models investigated as well as the experiments against the normalized

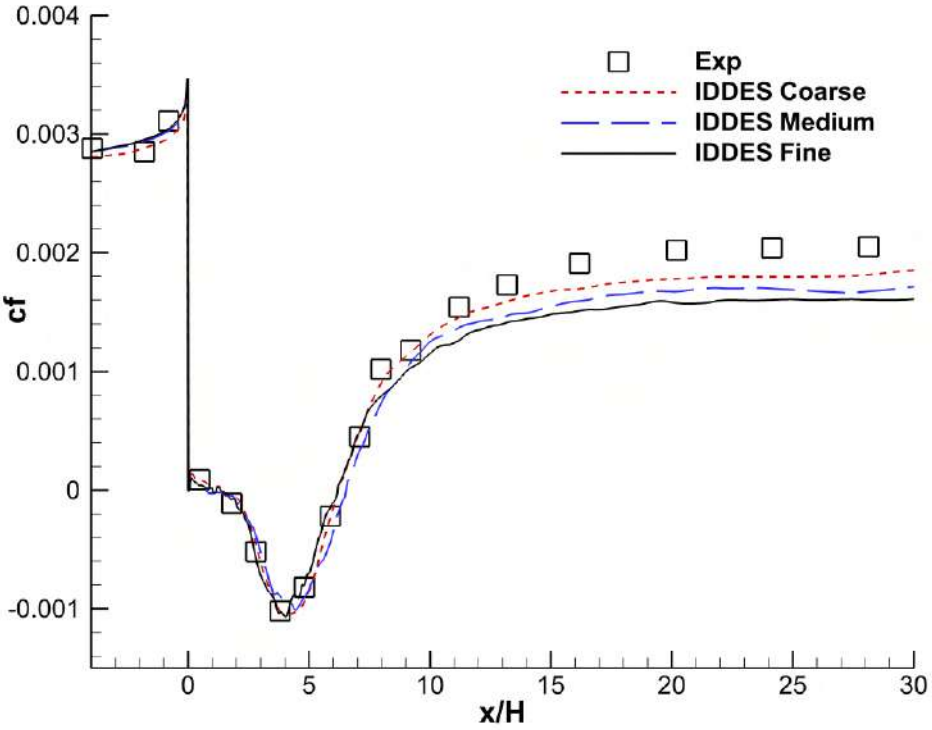

Figure 14: Mean skin friction coefficient distributions of IDDES

streamwise distance x/H are plotted in Figures 17, 18, and 19 for the coarse, medium, and fine meshes, respectively. The distributions of IDDES and PANS are in good agreement with the experimental data, although PANS slightly under-predicts c_f after reattachment in the medium and fine meshes. As was pointed out in the mesh study, WMLES completely misses the c_f in the separation zone with the coarse mesh, but shows much better agreement for the medium and fine meshes while the other models are able to capture this region with coarse grids. It is interesting to note that the WMLES performs well in the far downstream where good turbulent content is provided from the separating region. The most challenging task in the backward-facing step is to accurately predict the velocity distributions as well as to resolve the turbulent stresses profiles in both the separation and reattachment regions. The velocity profiles as well as the turbulent normal stresses $1/2(u'u' + v'v')$ and turbulent shear stress $u'v'$ distributions are presented in the following couple of Figures (20 to 28) for the three levels of resolu-

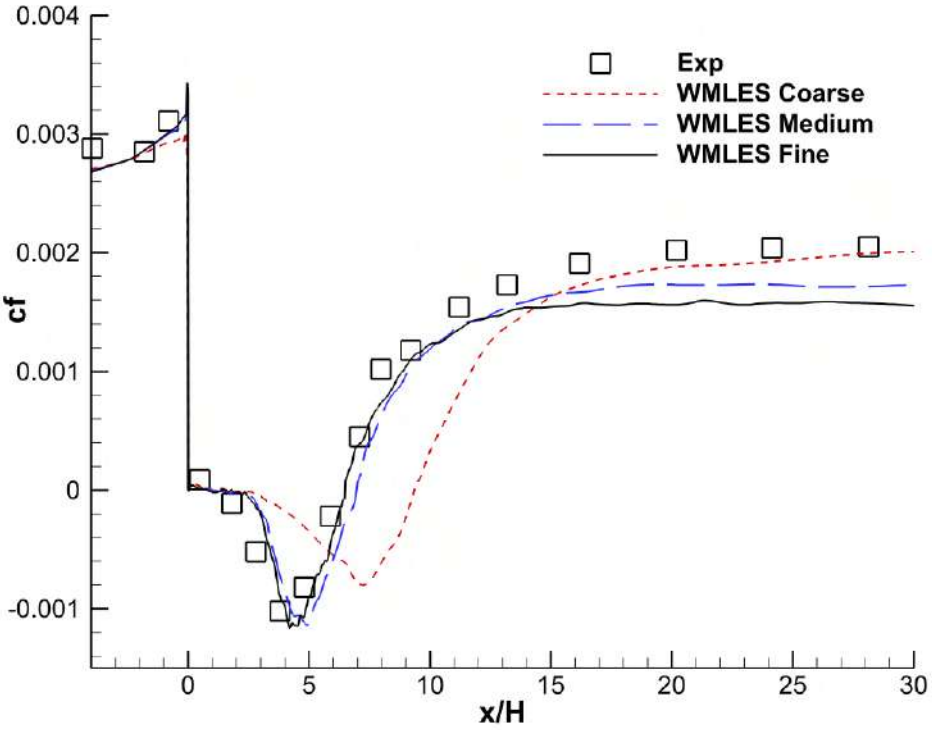

Figure 15: Mean skin friction coefficient distributions of WMLES

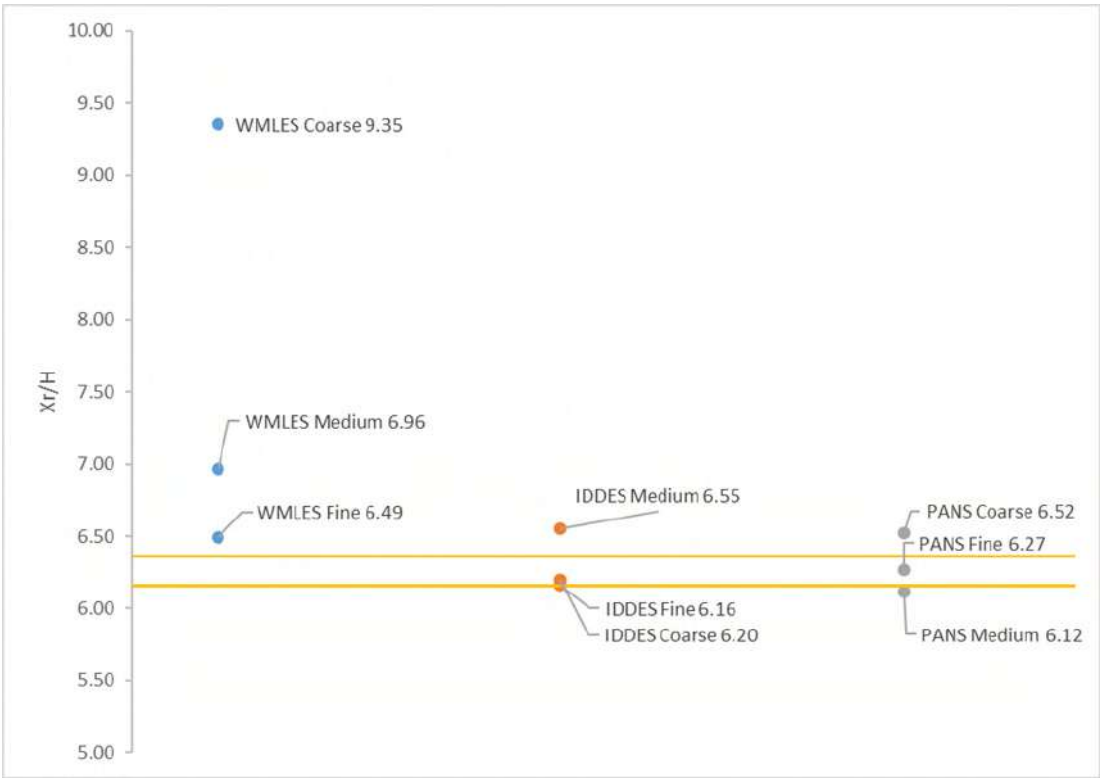

Figure 16: Reattachment length for the backward-facing step

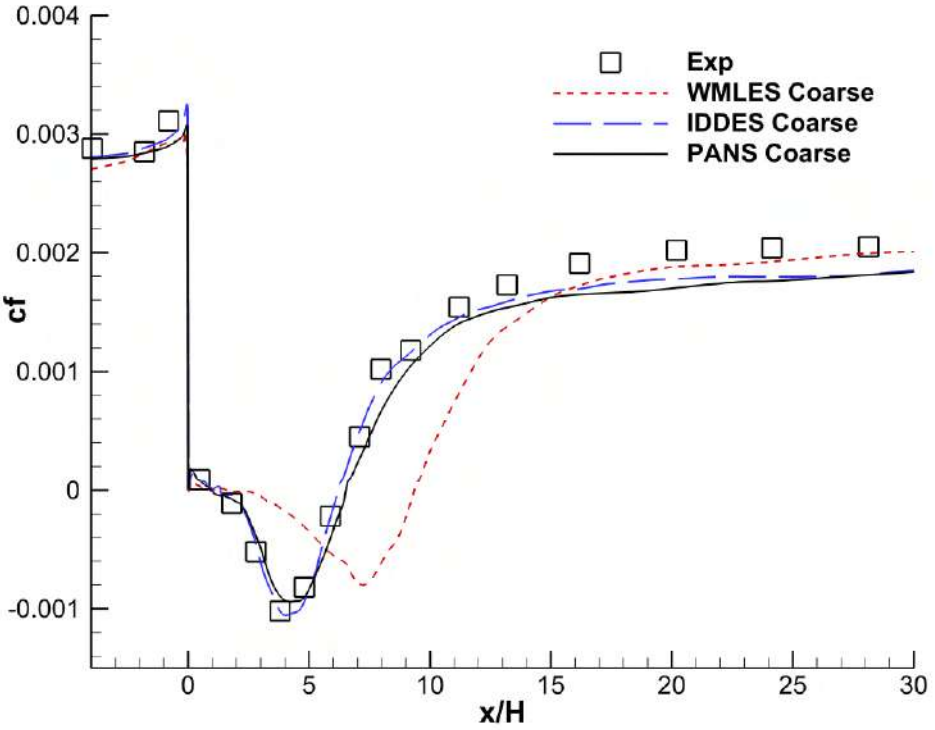

Figure 17: Mean skin friction coefficient for the various models on the coarse grid

tions. For the coarse mesh, PANS and IDDES have comparable levels of accuracy and are able to accurately predict the velocity profiles in both the separation and reattachment regions as shown in Figure 20. Velocities predicted by WMLES are way off for $6 < x/H < 10$ which corresponds to the region between the correct reattachment point and the calculated one. The turbulent normal stresses represented by $1/2(u'u' + v'v')$ are slightly better predicted by PANS compared to IDDES expect at $x/H = 6$ as can be seen in Figure 21 with both models having relatively good agreement with the experiments. On the other hand, WMLES is almost unable to resolve any normal stresses near the step while overpredicts it after reattachment. The shear stresses shown in Figure 22 shows similar trend to the normal ones. With the higher grid resolution of the medium mesh, the three models show good improvement, especially the proposed PANS model which is able to match the experimental velocity distributions shown in Figure 23. In addition, the turbulent normal stresses predicted by PANS on the medium mesh

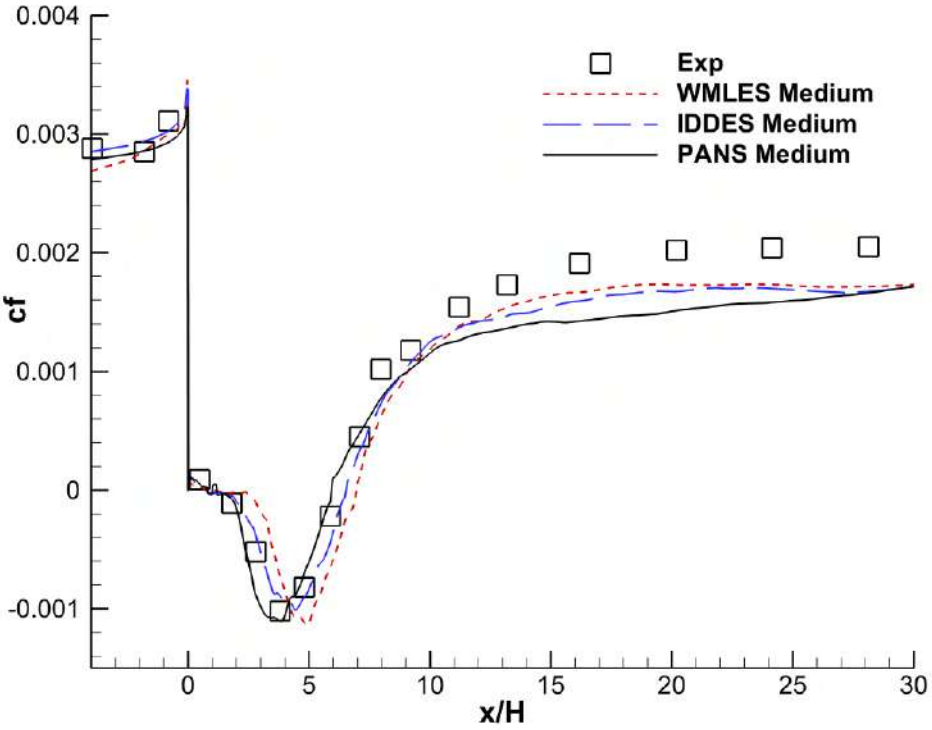

Figure 18: Mean skin friction coefficient for the various models on the medium grid

are considerably closer to the experiments then IDDES is. Surprisingly, the turbulent shear stresses show better agreement with the experiments for PANS only in the region $y/H < 1$, while IDDES is more accurate for $y/H > 1$ as seen in Figure 25. Going to the finest mesh, velocities predicted by PANS and IDDES are almost identical to the medium mesh, thereby showing grid independence. Both solutions are already a close match to the experimental data. The velocity distribution predicted by WMLES also stabilized with the earliest locations ($x/H = 1$ and $x/H = 2$) showing some deficiencies of the model at such location. The turbulent normal stresses show improvement on the finest grid with PANS keeping the upper hand on IDDES for most location as shown in Figure 27. WMLES is still lagging in resolving the normal stresses. For the turbulent shear stresses on the fine mesh in Figure 28, PANS shows better agreement with the experiment then IDDES. Overall, both PANS and IDDES models are able to

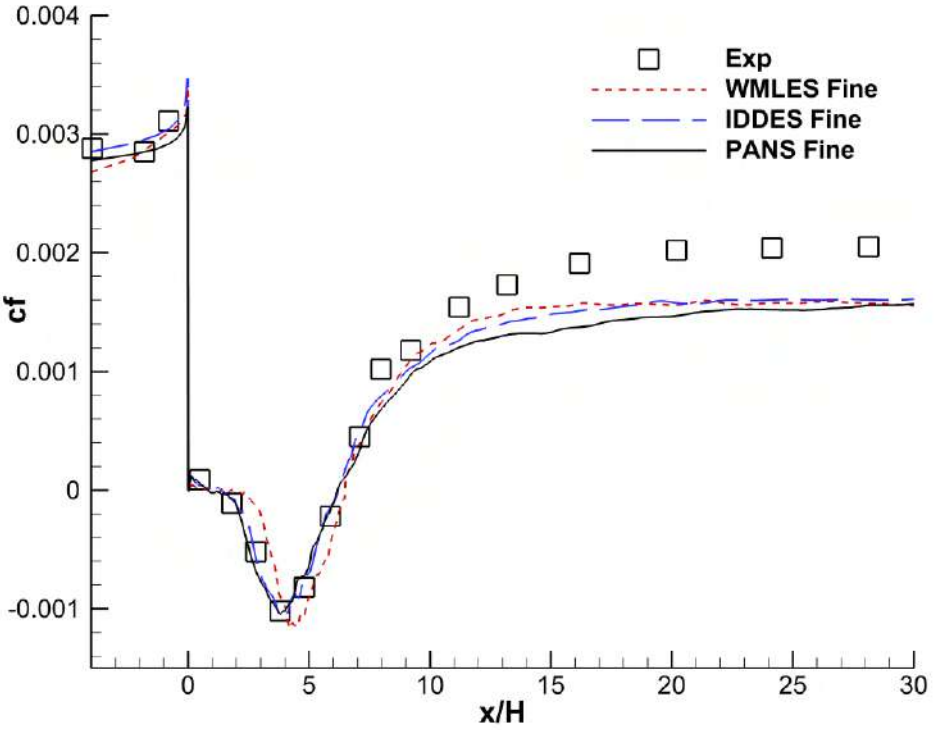

Figure 19: Mean skin friction coefficient for the various models on the fine grid

accurately predict the velocity profiles, turbulent normal stresses, and turbulent shear stresses. However, it was seen that IDDES only performs better on coarser grids, while PANS is much more accurate on finer grids. This behavior may be attributed to the fact that in coarser grids, more modelling is performed with the IDDES being based on the well calibrated two-equation k-ω SST RANS model. However, with finer grids, the contribution of the modelling part is much lower, allowing the proposed PANS model to resolved some part of the boundary, otherwise modeled by IDDES. It should be noted that although the results of PANS and IDDES seem to have stabilized, WMLES still seems to be grid dependent. This is not an issue at all here, since an objective of this study is to allow the model to seamlessly adjust its parameters to resolve as much scales as possible for any given grid. This is of course not an option with WMLES, which even though is a type of hybrid model, still has grid requirement similar to LES in region away from walls. To better visualize the resolved flow structures, velocity contours

are plotted on iso-surfaces of the Q-criterion at $Q = 1e^5$ in Figures 29, 30, and 31 for the coarse, medium, and fine mesh, respectively. It can be clearly seen that more structures are resolved with finer meshes for the PANS model. The same behavior is also seen and obviously expected for WMLES and IDDES as finer grids are capable of capturing even smaller scales. It is interesting to note however, that PANS and IDDES are able to resolve considerably more structures than the WMLES for the three mesh densities considered as shown in the below figures. Also, it can be clearly seen from Figure 31 that, for the fine mesh, PANS is able to resolve even more structures than IDDES. This is another advantage of the proposed model over IDDES which was specifically developed and extensively calibrated for cases like the backward-facing step. The reason behind this, is that IDDES has strong boundary layer shielding keeping it in RANS even for very fines meshes. PANS on the other hand, is able to resolve part of the boundary layer, if allowed by the grid size.

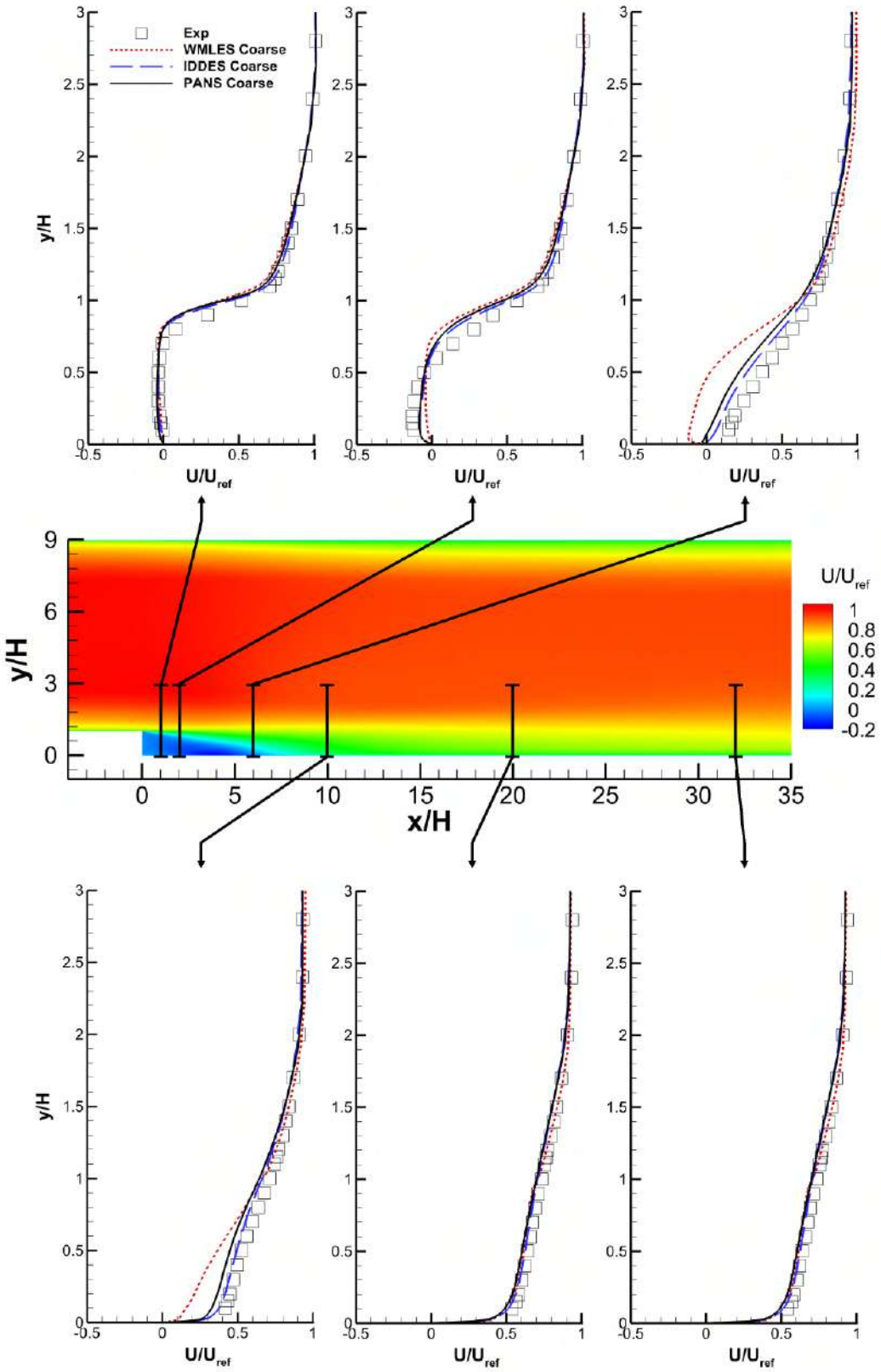

Figure 20: Mean streamwise velocity profiles on the coarse mesh (contours are shown for PANS)

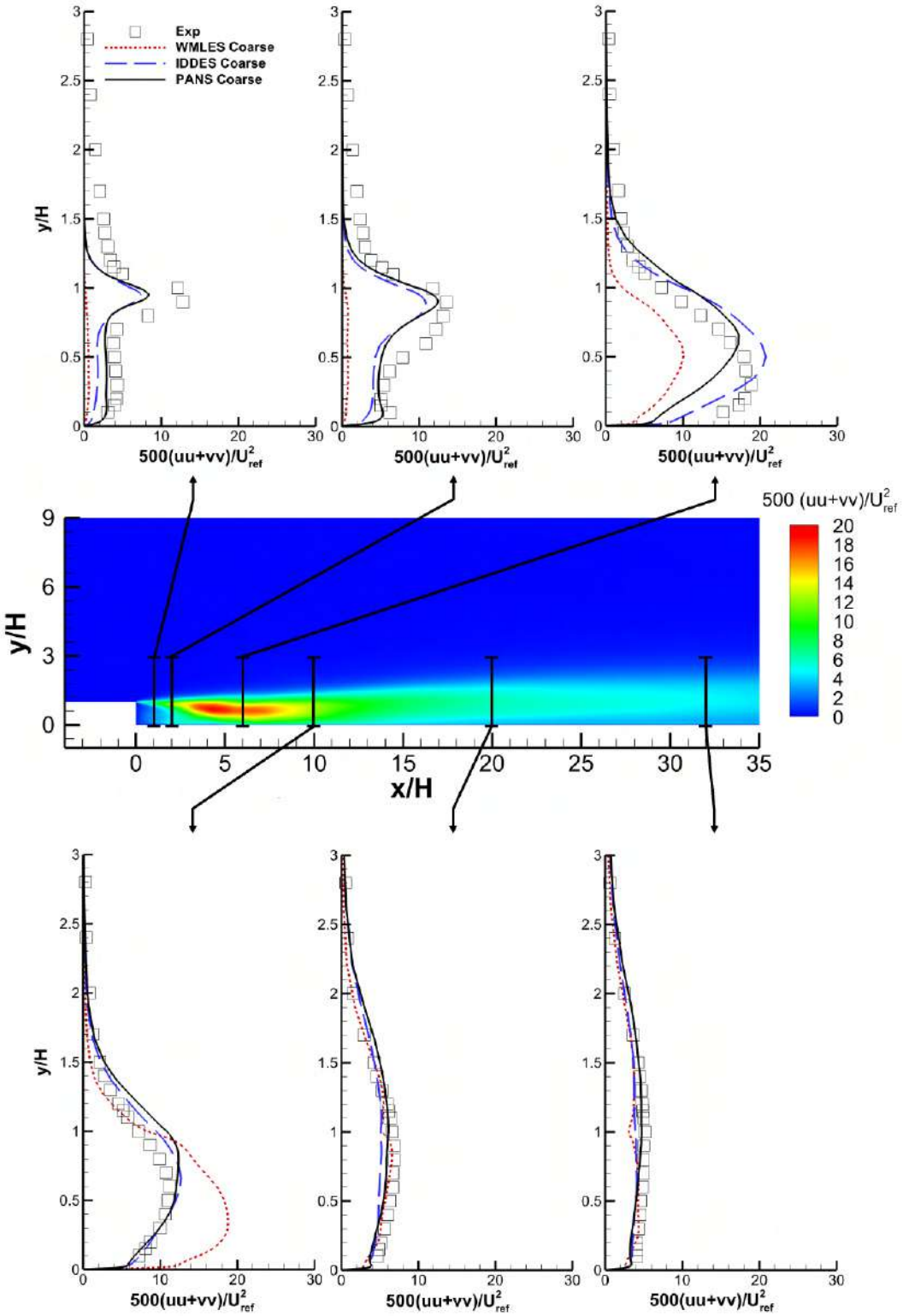

Figure 21: Turbulent normal stress profiles on the coarse mesh (contours are shown for PANS)

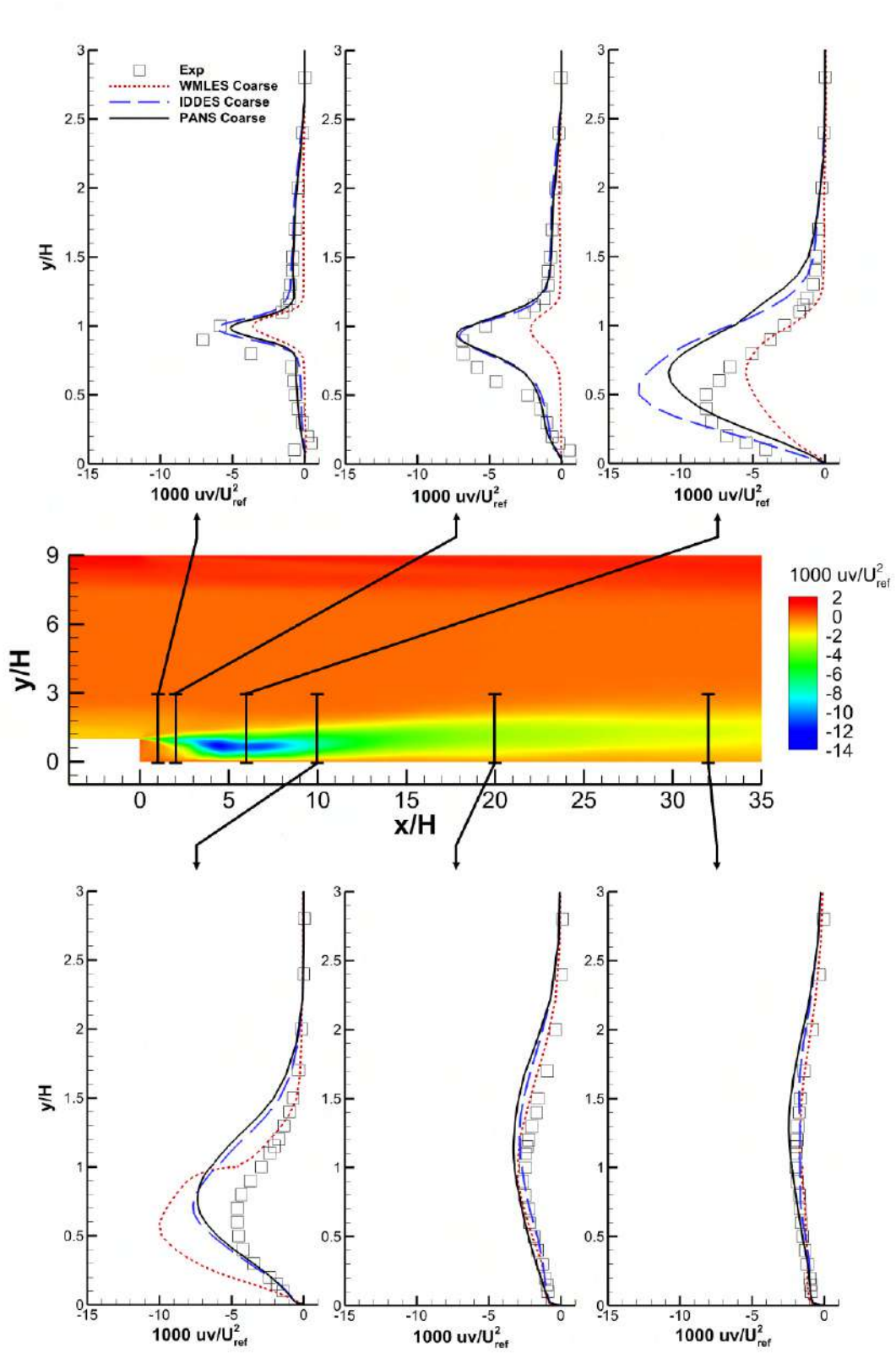

Figure 22: Turbulent shear stress profiles on the coarse mesh (contours are shown for PANS)

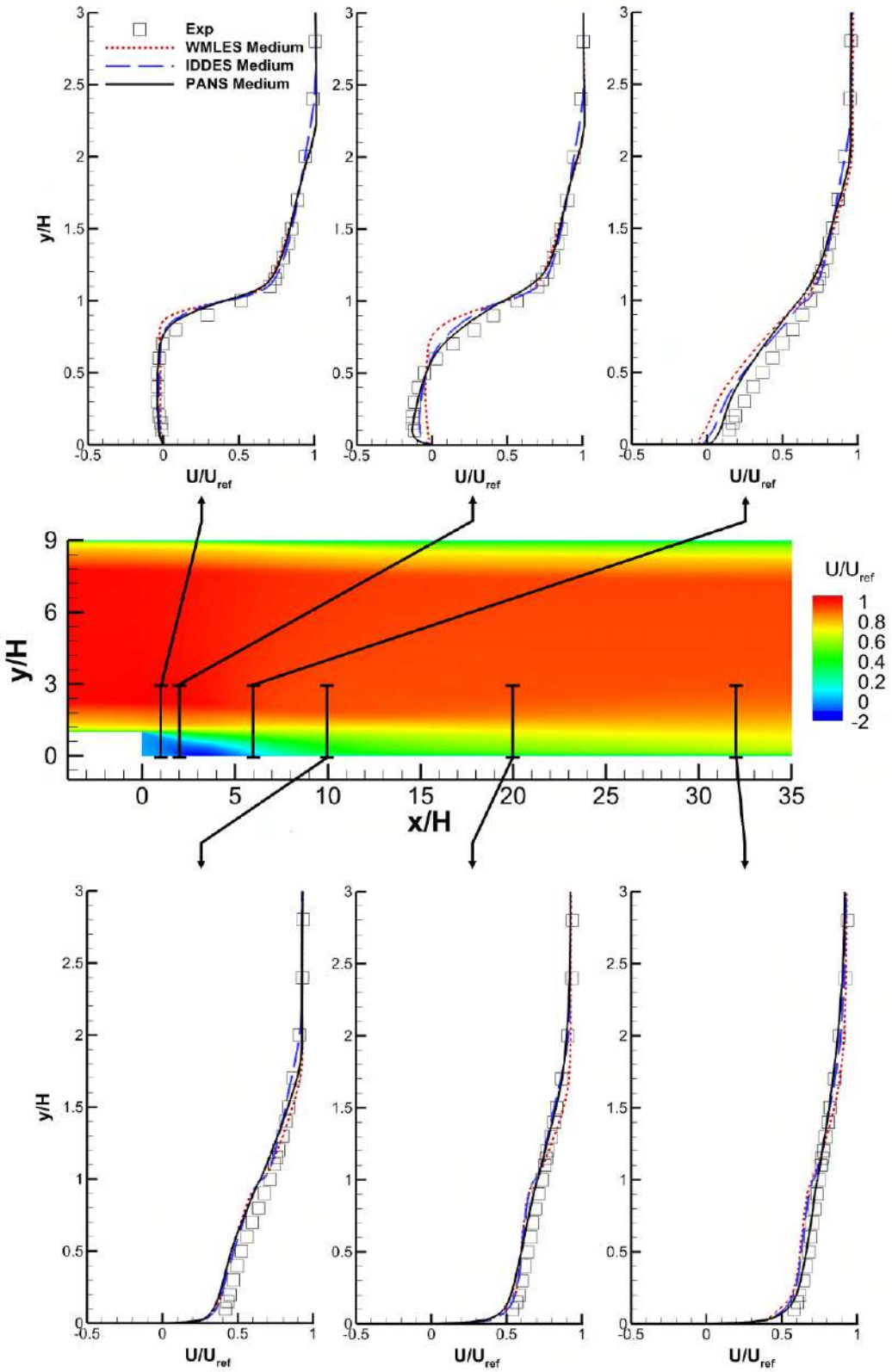

Figure 23: Mean streamwise velocity profiles on the medium mesh (contours are shown for PANS)

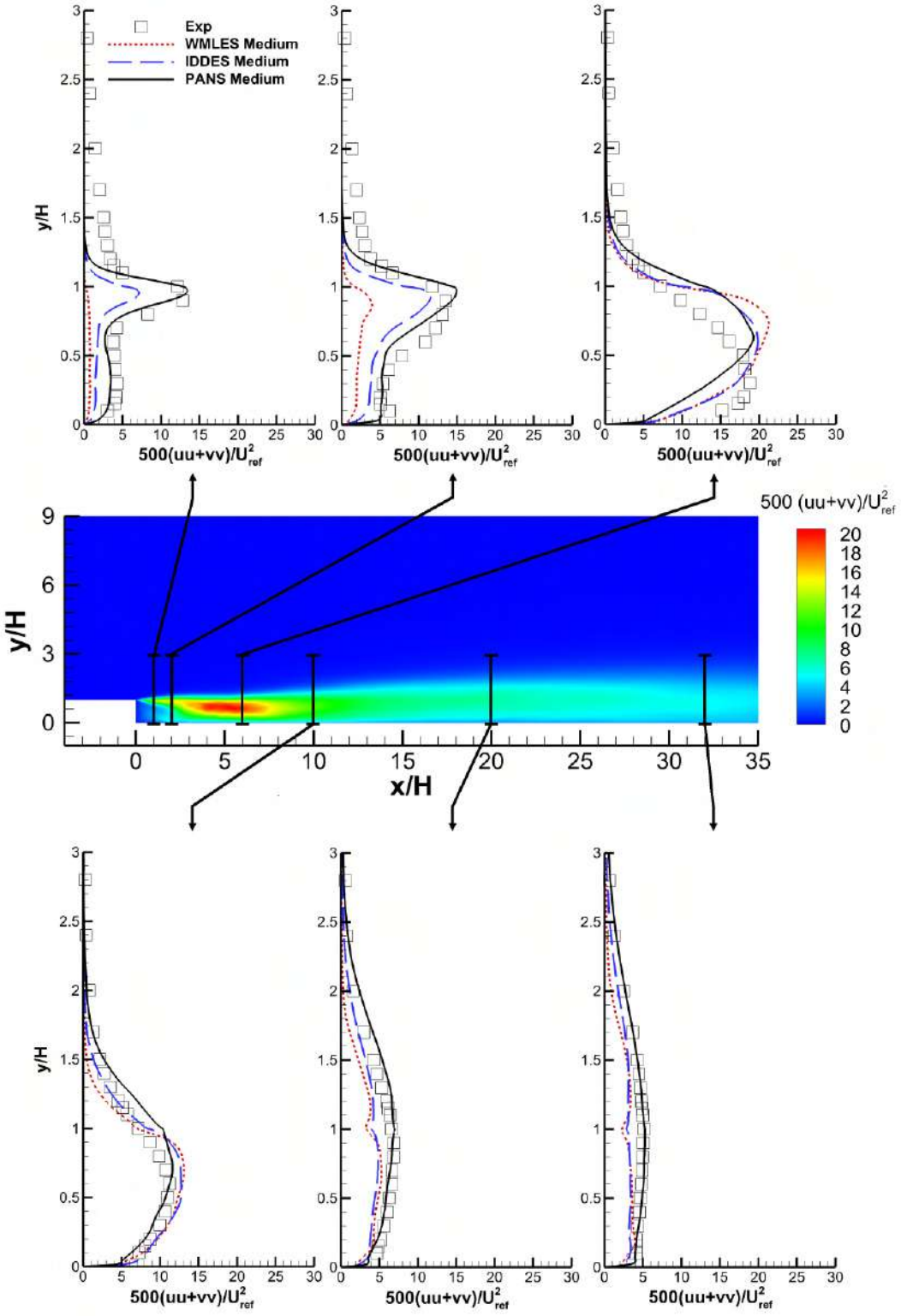

Figure 24: Turbulent normal stress profiles on the medium mesh (contours are shown for PANS)

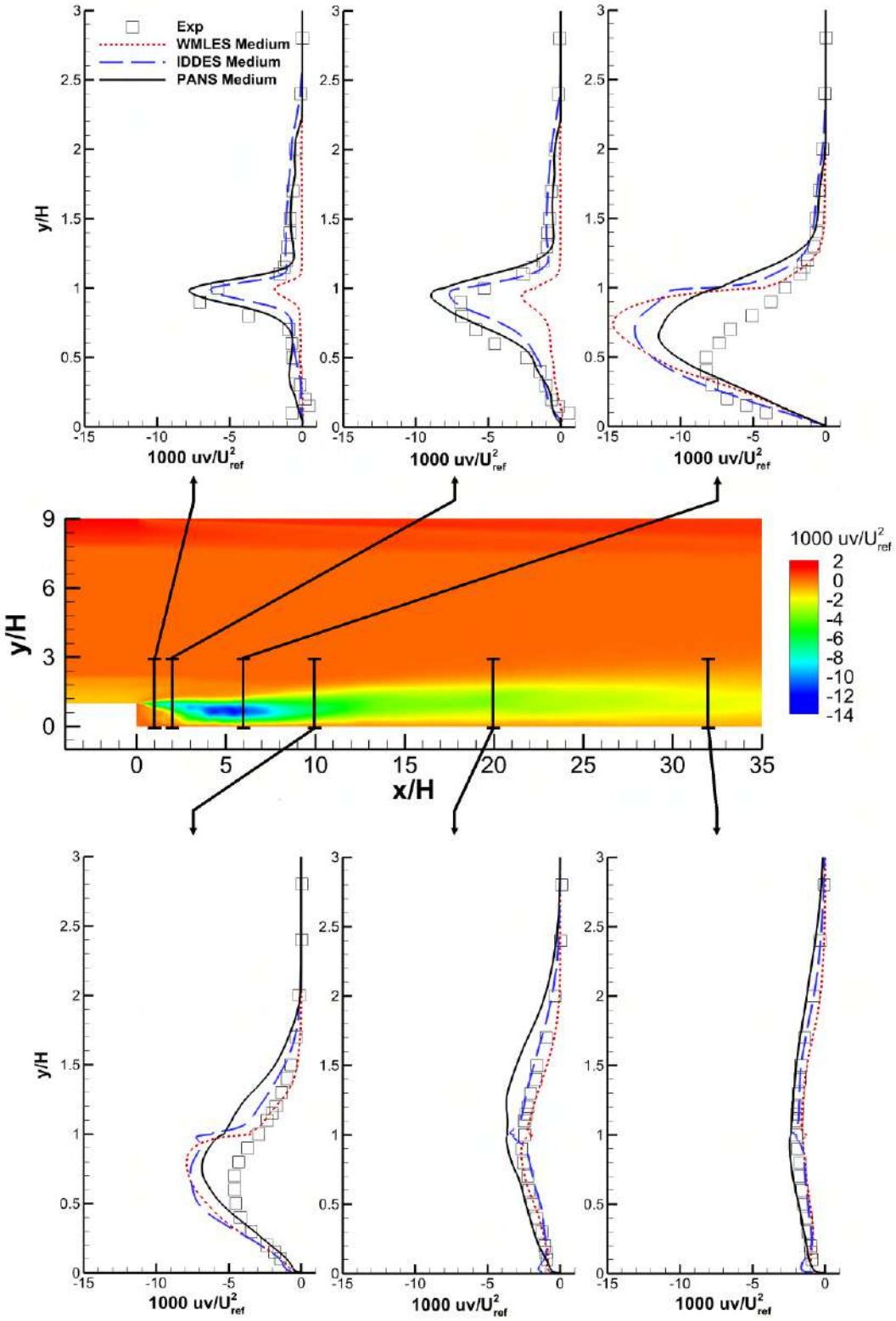

Figure 25: Turbulent shear stress profiles on the medium mesh (contours are shown for PANS)

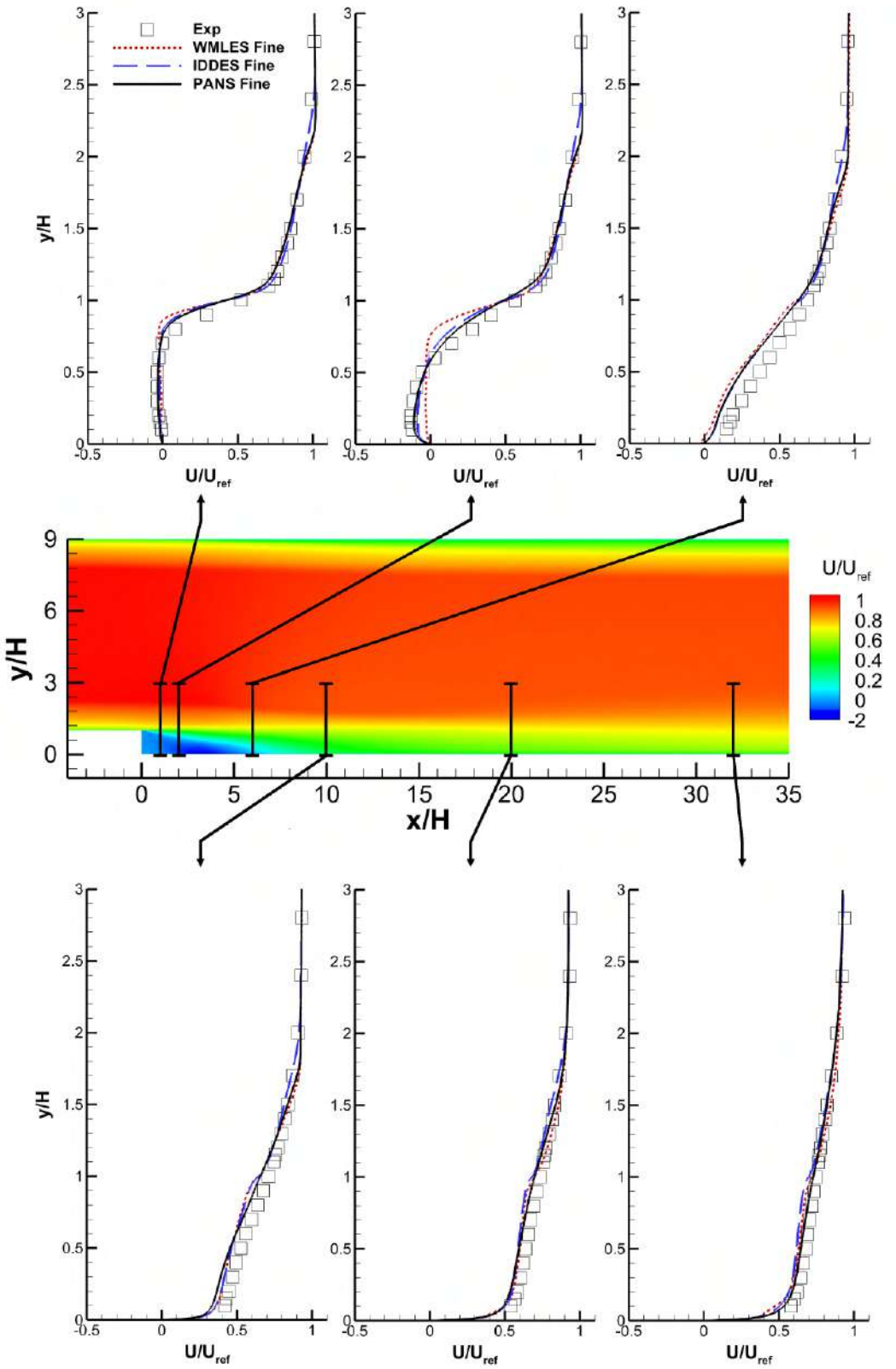

Figure 26: Mean streamwise velocity profiles on the fine mesh (contours are shown for PANS)

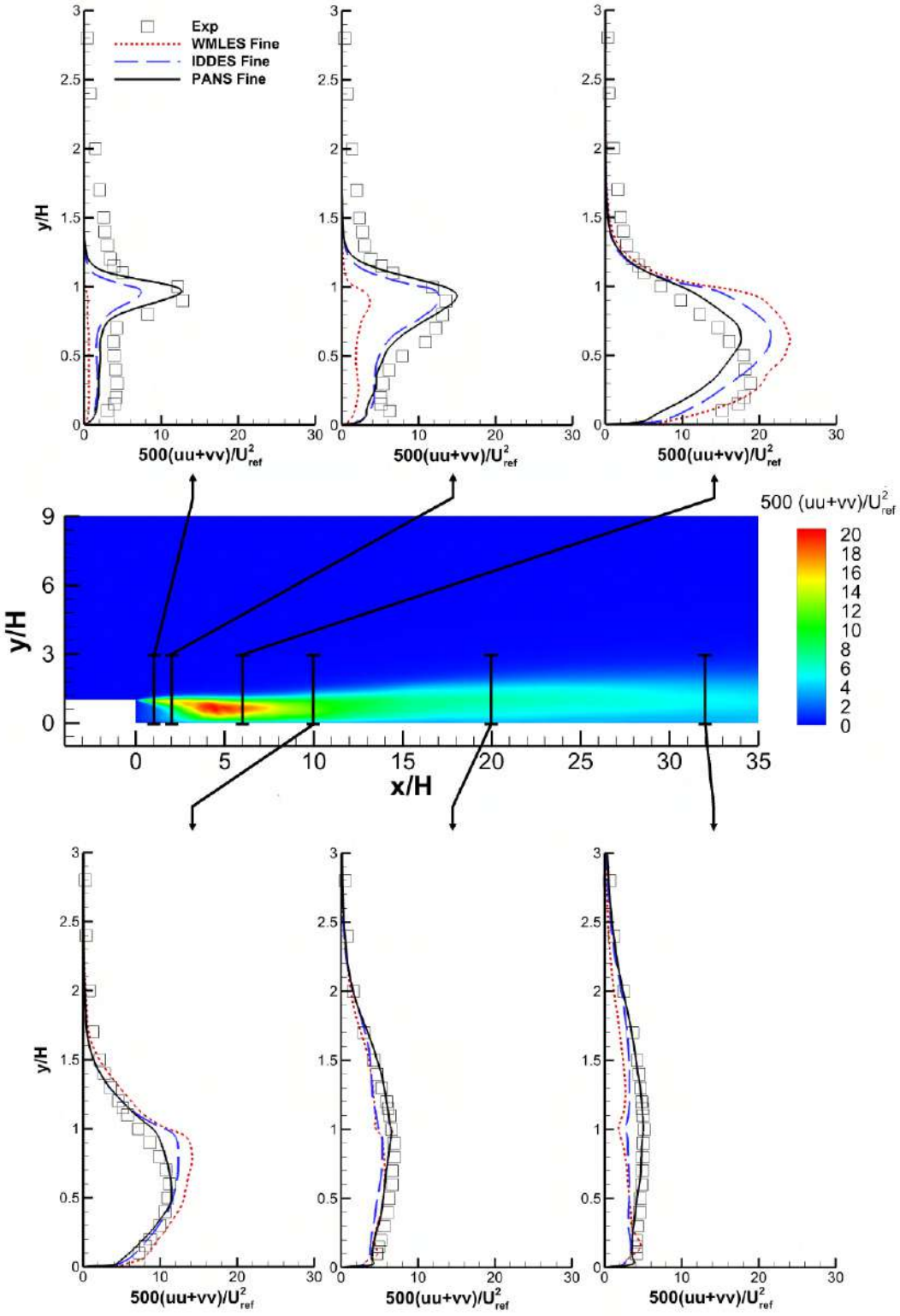

Figure 27: Turbulent normal stress profiles on the fine mesh (contours are shown for PANS)

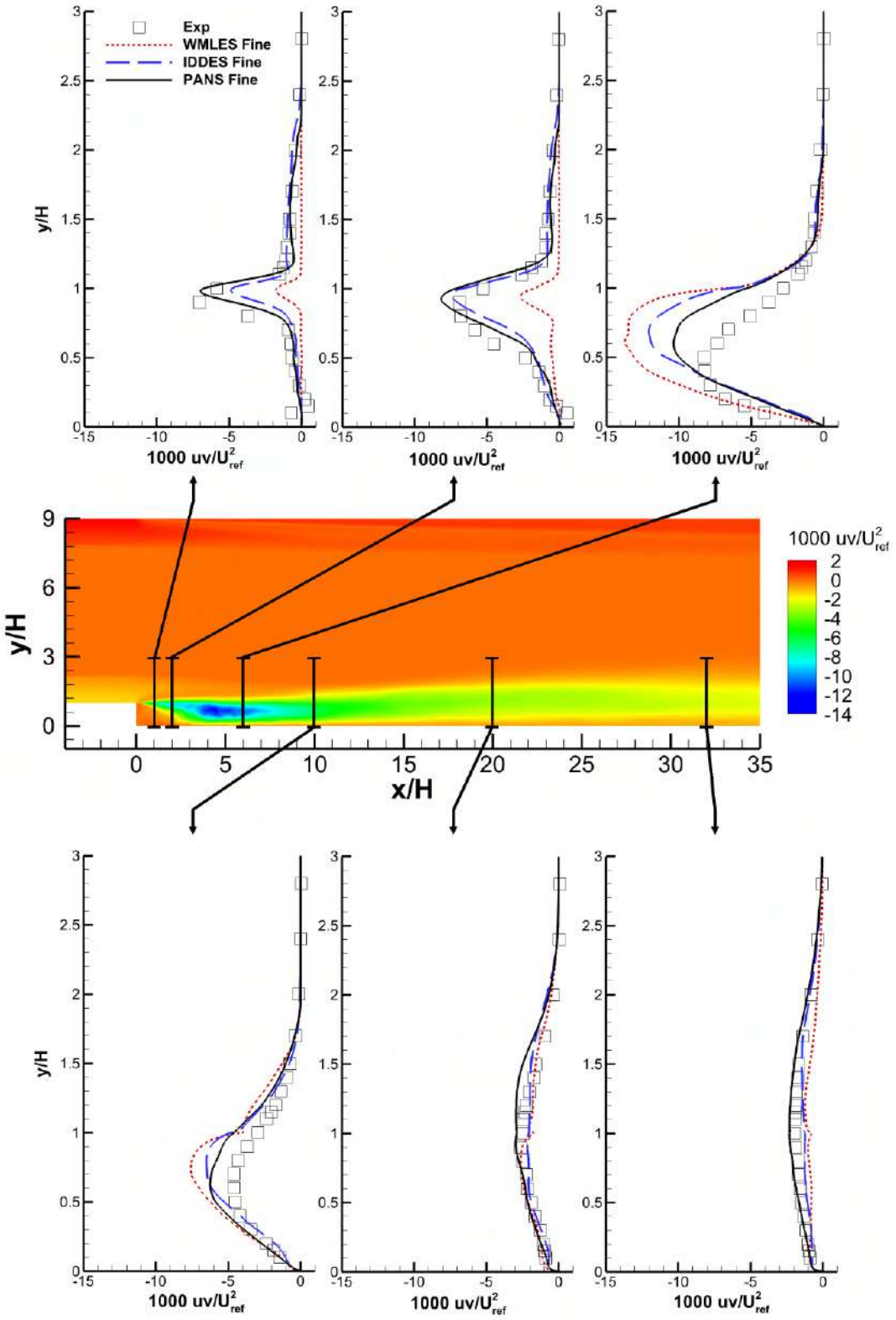

Figure 28: Turbulent shear stress profiles on the fine mesh (contours are shown for PANS)

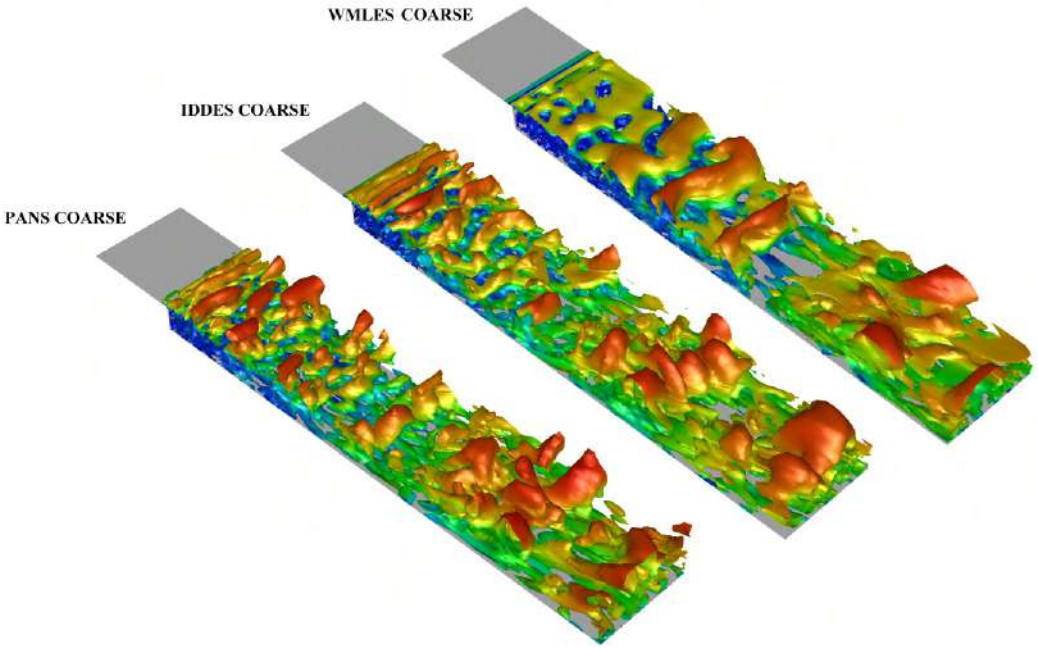

Figure 29: Velocity contours on isosurfaces of $Q = 1e^5$ for PANS (left), IDDES (middle), and WMLES (right) for the low density mesh

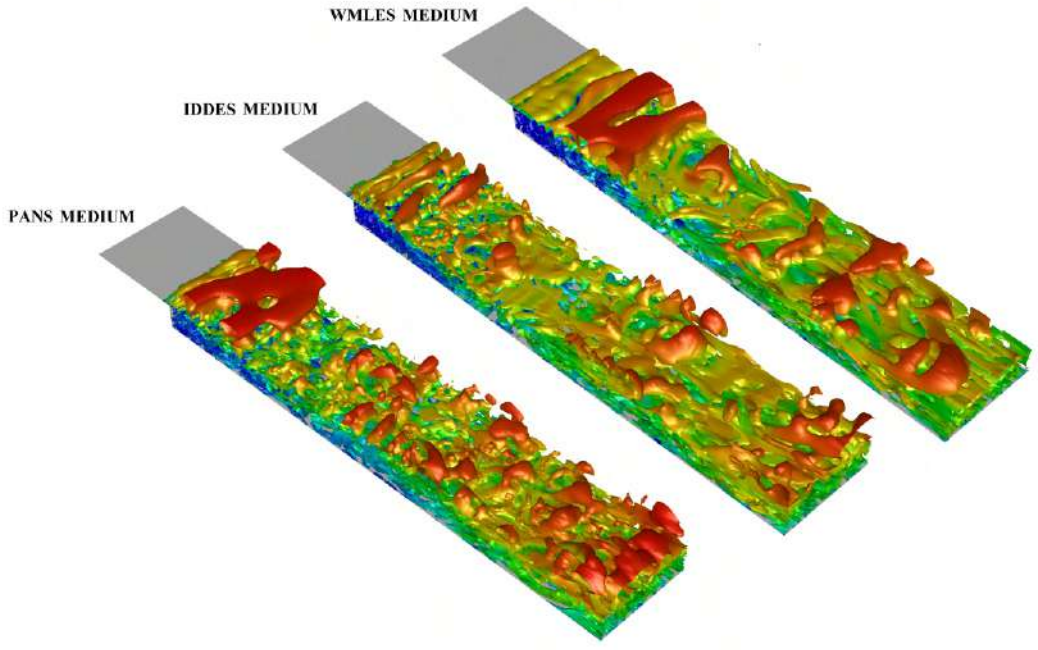

Figure 30: Velocity contours on isosurfaces of $Q = 1e^5$ for PANS (left), IDDES (middle), and WMLES (right) for the medium density mesh

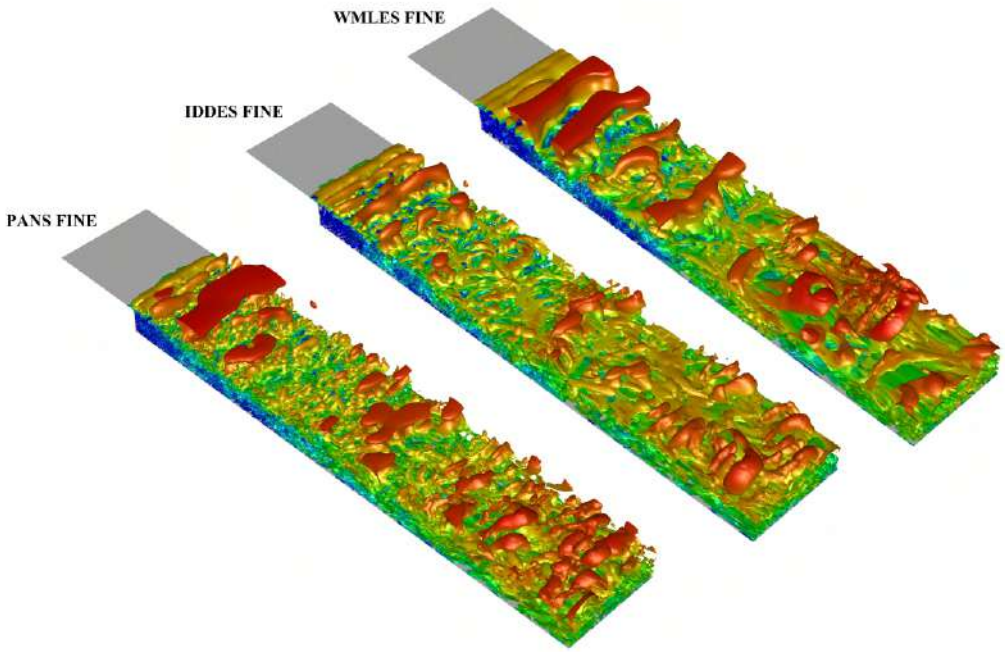

Figure 31: Velocity contours on isosurfaces of $Q = 1e^5$ for PANS (left), IDDES (middle), and WMLES (right) for the high density mesh

5.2 Ahmed Body

The results of the Ahmed body simulations are reported in this section.

5.2.1 Sampling Time

A sampling time study is also performed for the Ahmed body case. Being the proposed model, in this study, the effect of sampling time for the PANS model is presented here. In the same spirit as the backward-facing step, 2 locations are considered: one being on top of the slant and the other in the immediate body wake. Profiles of the averaged streamwise velocity U and mean streamwise velocity fluctuations $u - rms$ are shown against the wall-normal direction z at $x = -0.012m$ in Figure 32 and at $x = 0.038m$ in Figure 33. At both locations, the velocity profiles barely change after $0.12s$, however, velocity fluctuations require at least $0.2s$ to stabilize. Thus, all variables are averaged over a minimum of $0.2s$, or the equivalent of 8 flow-through the entire body.

5.2.2 Model Validation

The results of the Ahmed body are presented and compared with the experiments of Lienhart et al. (2002). First, the aerodynamic forces on the body walls are investigated. The drag and lift coefficients are calculated using Eq.(48) and Eq.(49), respectively.

$$C_d = \frac{2D}{\rho A U^2} \tag{48}$$

$$C_l = \frac{2L}{\rho A U^2} \tag{49}$$

Where, ρ is the fluid density, A is the reference surface area, U is the freestream velocity, D is the drag force, and L is the lift force. These coefficients are time averaged and reported in Table 4 for the three models considered in the cur-

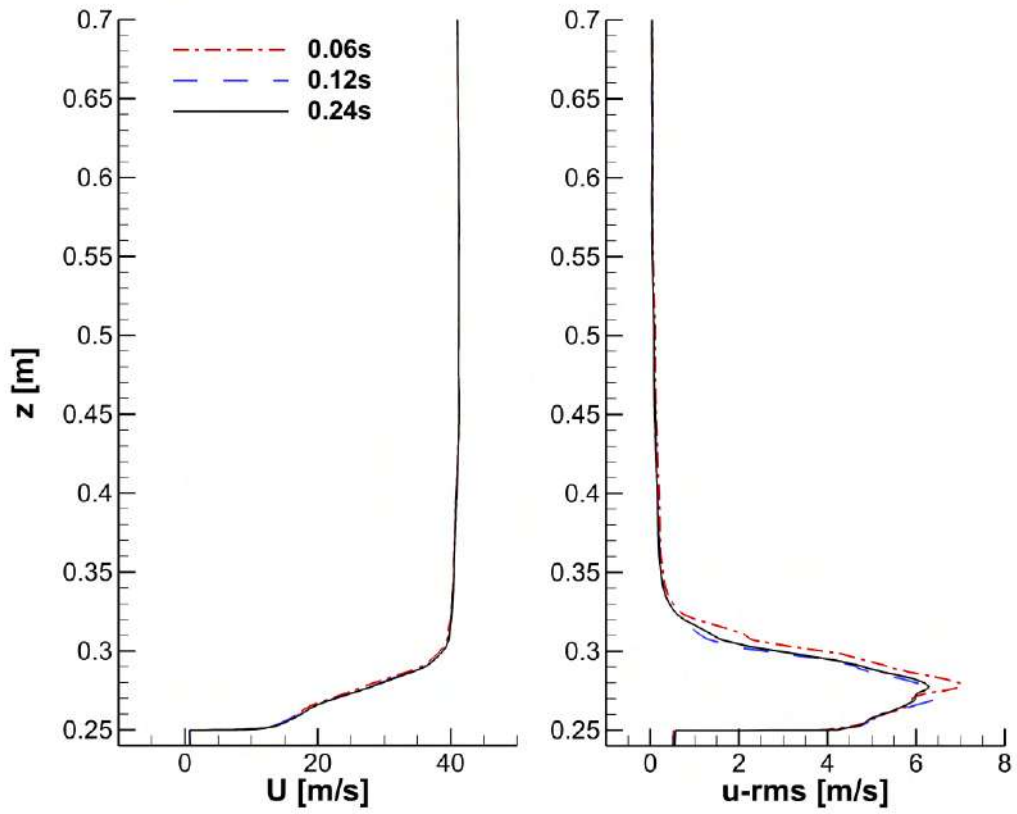

Figure 32: Convergence of velocity and streamwise velocity fluctuations for x = -0.012m

rent study, alongside the experimental values for comparison. Lift coefficients are computed with good accuracy for all three models below 3% error, with PANS showing the closest agreement by a slight margin. On the other hand, drag coefficients are all over-predicted with WMLES having the closest value to the experiments. It is also interesting to note that the values of drag coefficients predicted by IDDES (0.330) and WMLES (0.311) are in very good agreement with the values computed by Serre et al (2013). with the original DES-SST yielding $c_d = 0.343$ and LES with Near Wall Modelling (LES-NWR) yielding $c_d = 0.317$ .Even though the solved equations are not exactly the same in both studies, The different models in the same family of hybrid models were able to predicts similar values for c_d. This constitutes an additional validation of the solver, thereby increasing the author's confidence in the obtained results. Averaged velocity profiles in the streamwise U and wall normal directions W, are

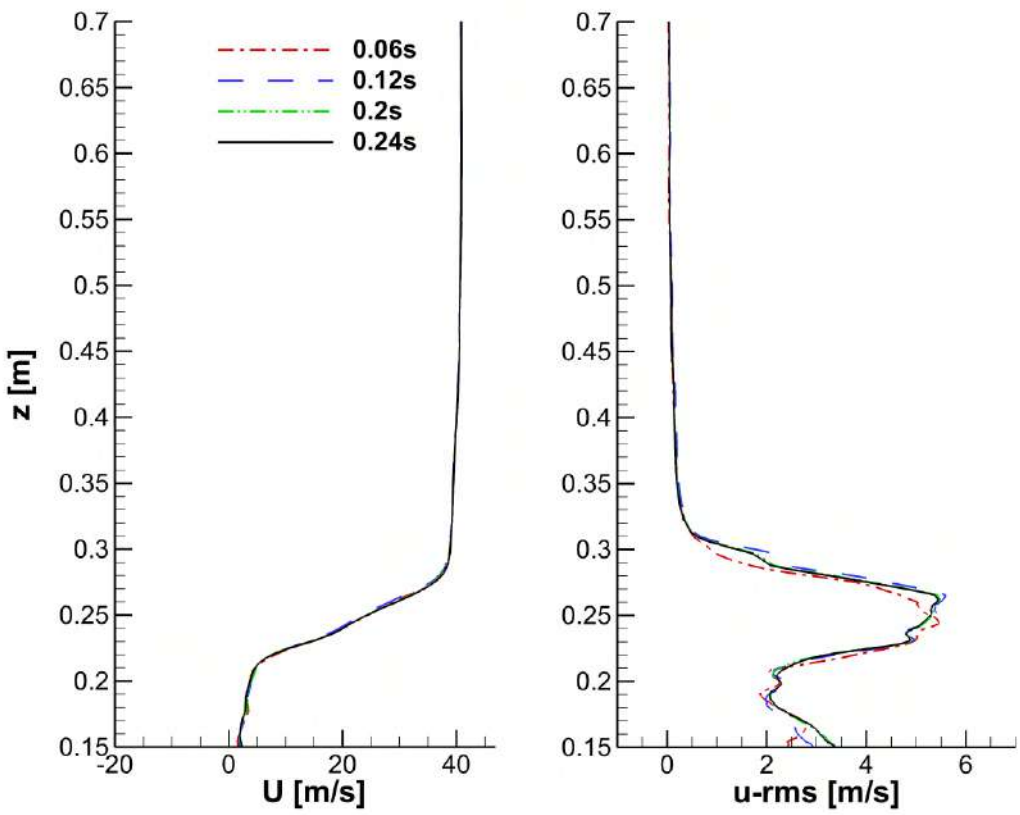

Figure 33: Convergence of velocity and streamwise velocity fluctuations for x = 0.038m

Table 4: Lift and Drag coefficients on the Ahmed body

	Exp.	WMLES	IDDES	PANS
c_d	0.298	0.311 (4.34%)	0.330 (10.69%)	0.320 (7.38%)
c_l	0.345	0.354 (2.71%)	0.336 (-2.70%)	0.353 (2.28%)

shown in Figures 34 and 35 respectively. It can be seen that the three models show excellent agreement with the experimental results with no model having the upper hand at all locations. The mean streamwise velocity fluctuations $u - rms$ and and wall normal velocity fluctuations $w - rms$ are shown in Figures 36 and 37, respectively. It is clear from these figures, that WMLES under-predicts the velocity fluctuations in both directions at all the locations considered, especially in the region $z > 0.2m$. On the other hand, PANS and IDDES show overall very good agreement with the experimental data. It is interesting to note, that

although both models are quite accurate, IDDES shows closer agreement in the region above the slant, while PANS is much more accurate in the body wake, especially in the far downstream. Contours of mean streamwise velocity U, mean

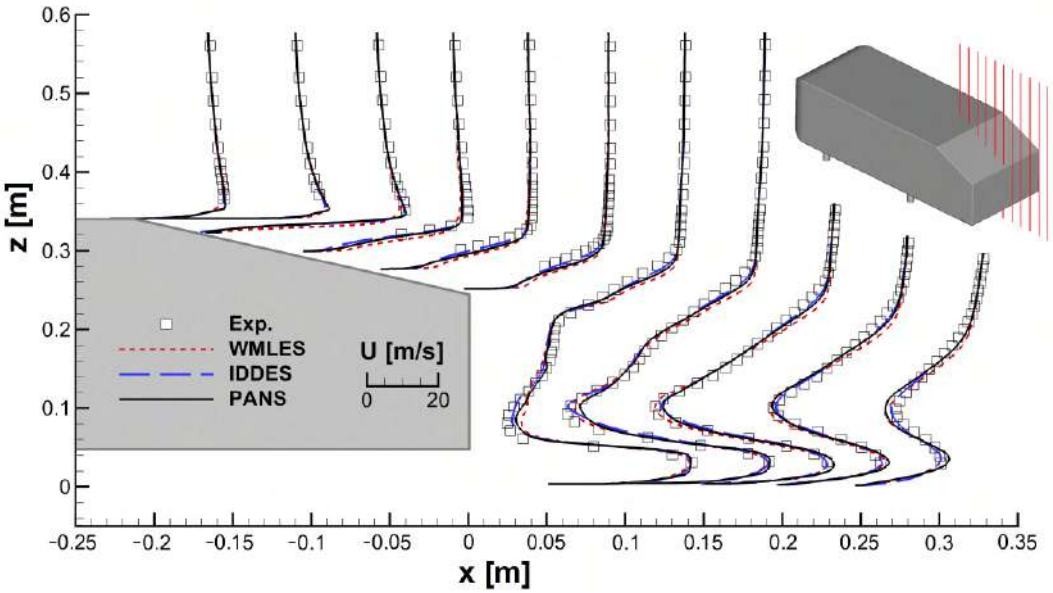

Figure 34: Profiles of the average streamwise velocity U over the Ahmed body

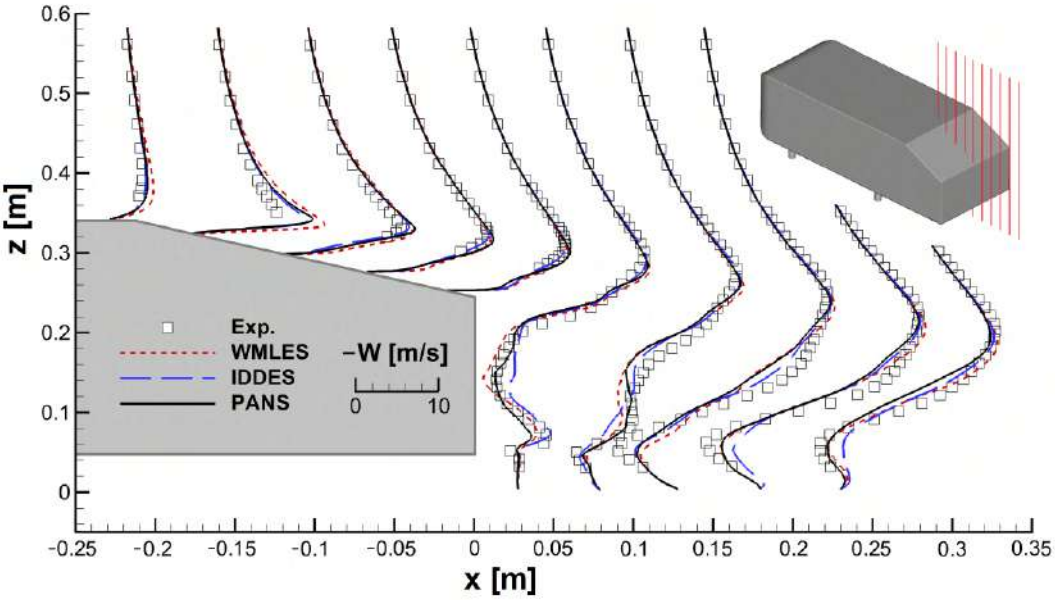

Figure 35: Profiles of the average wall normal velocity W over the Ahmed body

spanwise velocity V, mean wall normal velocity W, and mean streamwise velocity fluctuations $u'u'$ are plotted along with veloctiy vectors for downstream locations,

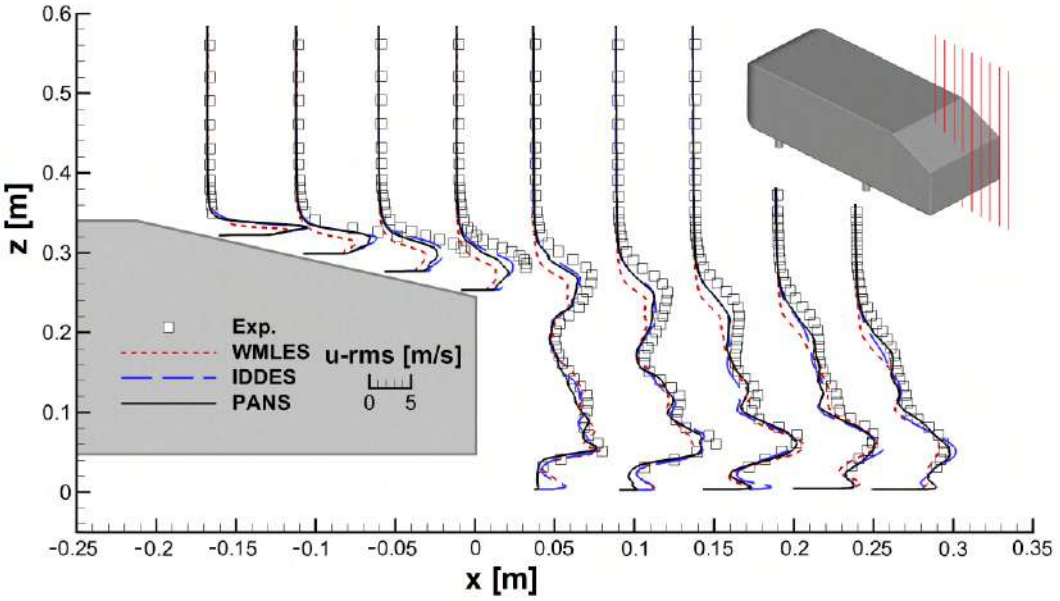

Figure 36: Profiles of the average streamwise velocity fluctuations $u - rms$ over the Ahmed body

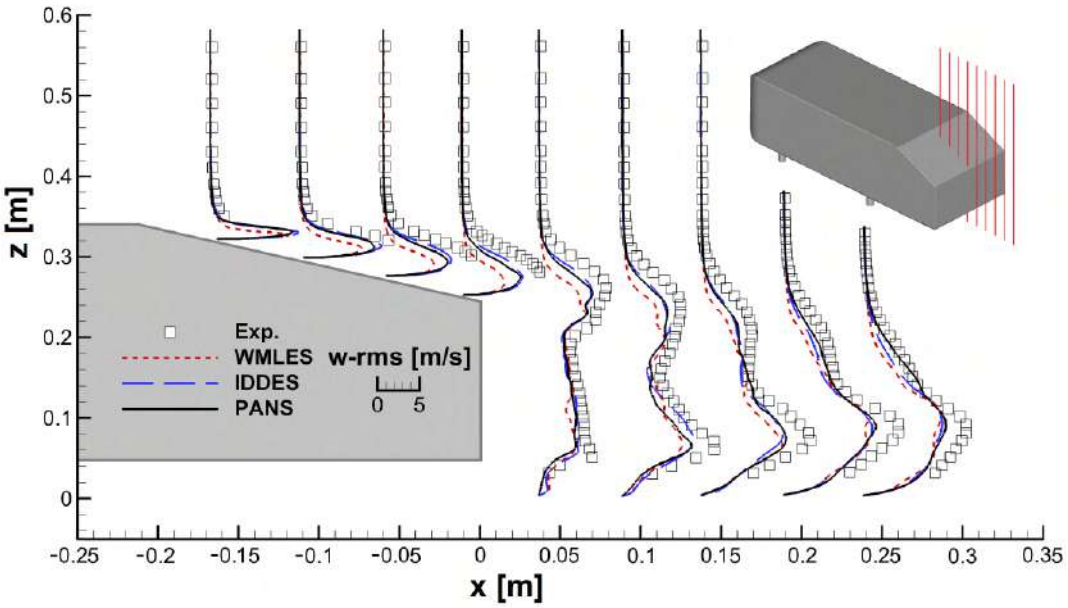

Figure 37: Profiles of the average wall normal velocity fluctuations $w - rms$ over the Ahmed body

in Figures 38, 39, 40, and 41, respectively. These plots show the spanwise distributions of the mentioned quantities, as opposed to the ones in Figures 34 to 37 that only show the symmetry plane, i.e., where $y = 0$ $[m]$. It can be seen from these plots that the three models are in good agreement with the experiments,

showing the fidelity of the proposed model in capturing the 3D effects in external aerodynamic cases. Contours of averaged streamwise velocity are shown in

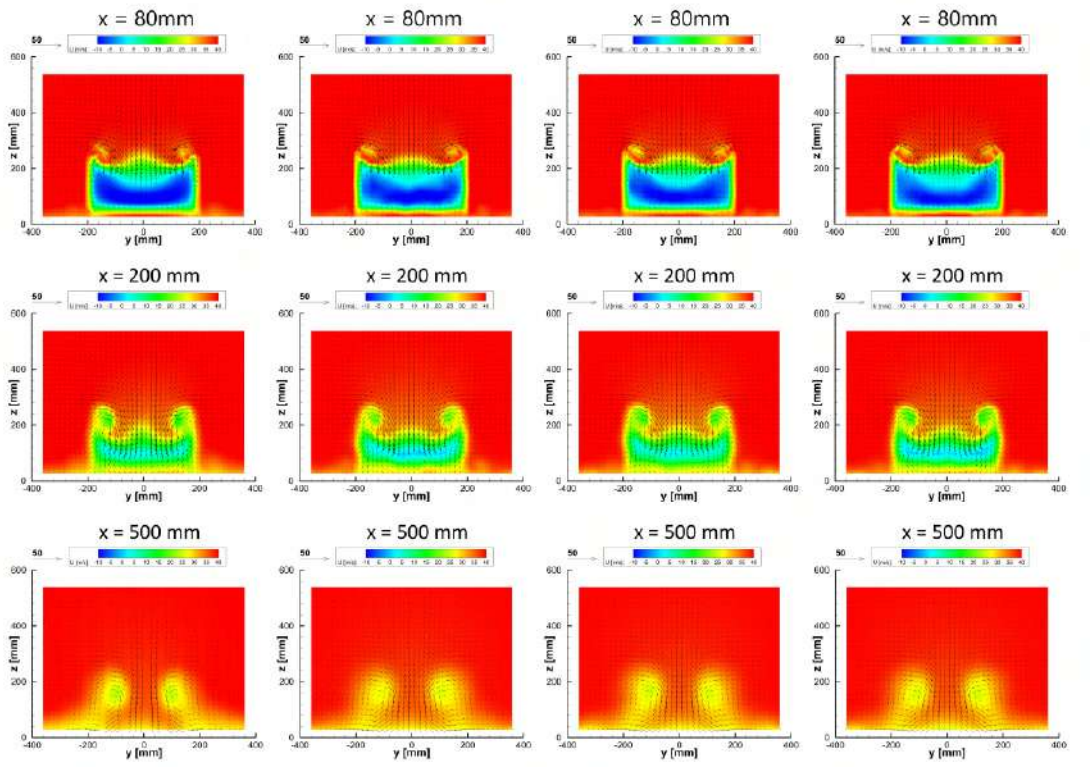

Figure 38: Contours of the average streamwise velocity U. From left to right: Exp., WMLES, IDDES, and PANS.

Figure 42, along with the mean velocity streamlines. It can be clearly seen that three models are able to predict the 2 recirculation regions in the body wake, with PANS and IDDES having slightly closer shapes with the experiments. The experimental data does not show the near wall statistics, but it can also be seen from Figure 42, that the separation region on the slant for WMLES is smaller than the ones predicted by PANS and IDDES. Velocity contours are plotted on iso-surfaces of the Q-criterion at $Q = 1e^5$ in Figure 43 for the PANS, WMLES, and IDDES. The resolved structures are clearly seen for all models downstream the slant. It is interesting to note however, that PANS does not resolve any structures prior to separation on the slant. This indicates that all the scales at such locations are modelled. This is not necessarily a deficiency of the model, keeping in mind that the lift and drag coefficients predicted by PANS are both closer

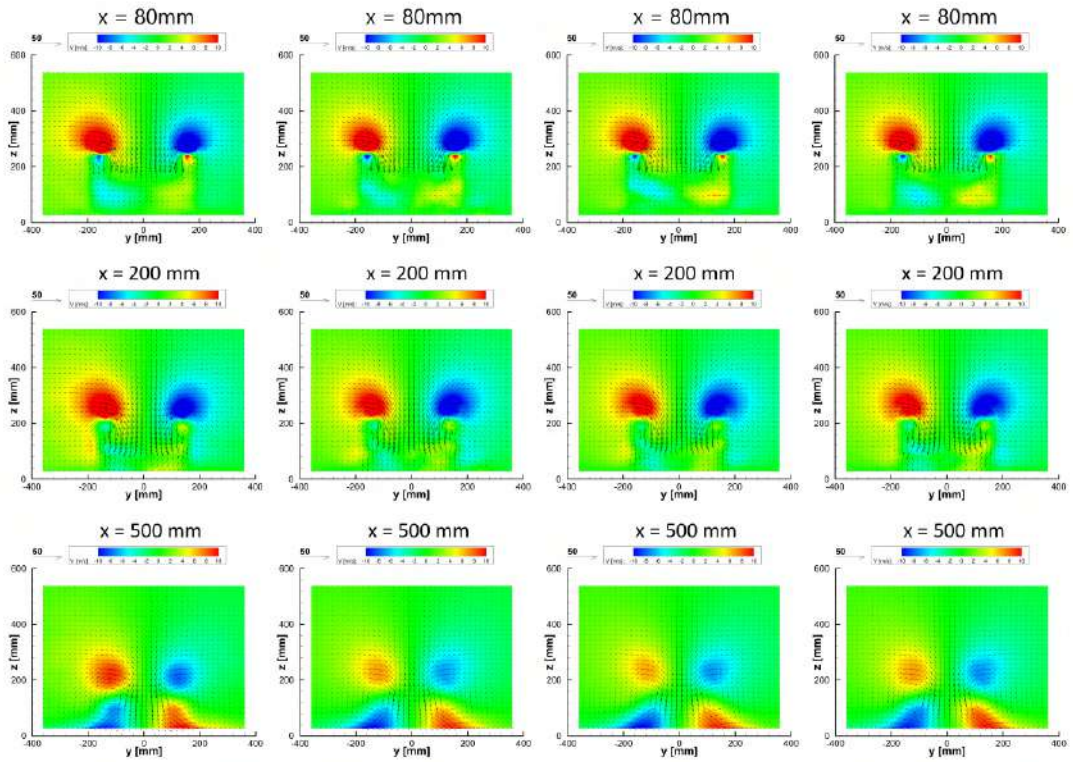

Figure 39: Contours of the average spanwise velocity V. From left to right: Exp., WMLES, IDDES, and PANS.

to the experiments than IDDES. Further investigation should be carried out to determine the appropriate amount of balance between modelling and resolving at such locations. Overall, for external aerodynamic flow, like the Ahmed body case here, it was seen that the proposed PANS model is able to show good agreement with the experiments. Although, the mesh used in this study is considered to be a fine one for the current case, it is expected that PANS should be able to yield much better results than other hybrid approaches on coarser grids. This is mainly because, the proposed model can switch to a full RANS formulation, even in the free shear region, which is not possible for other models, like the WMLES.

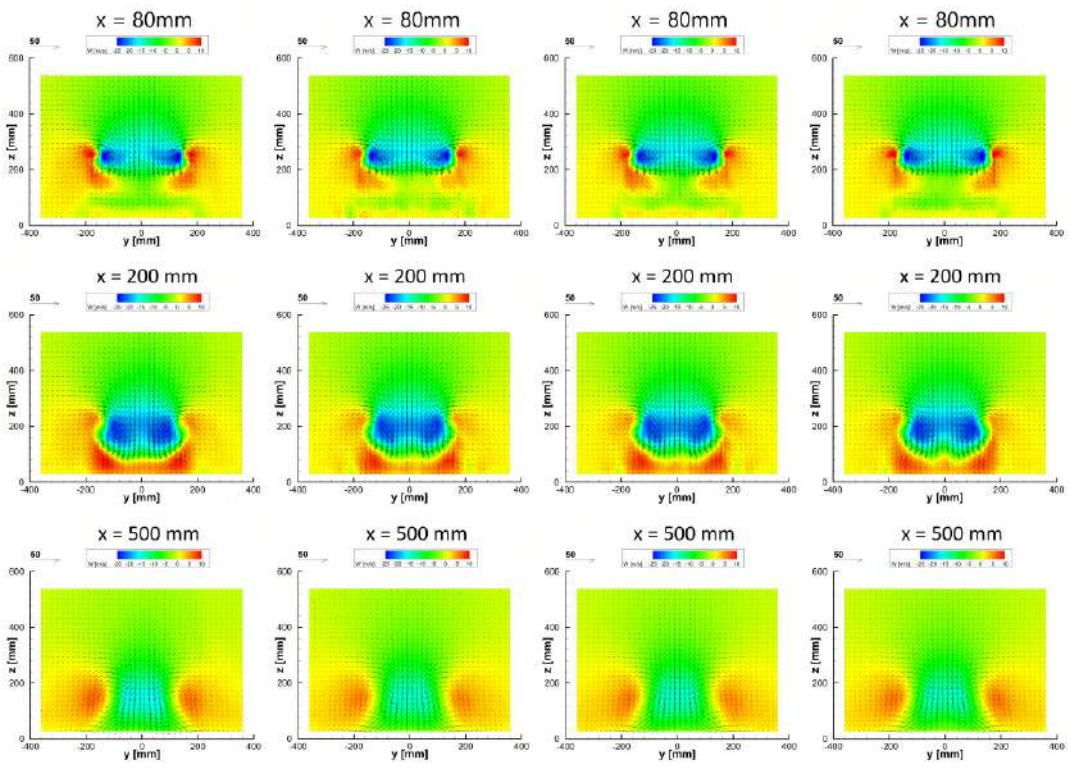

Figure 40: Contours of the average wall normal velocity W. From left to right: Exp., WMLES, IDDES, and PANS.

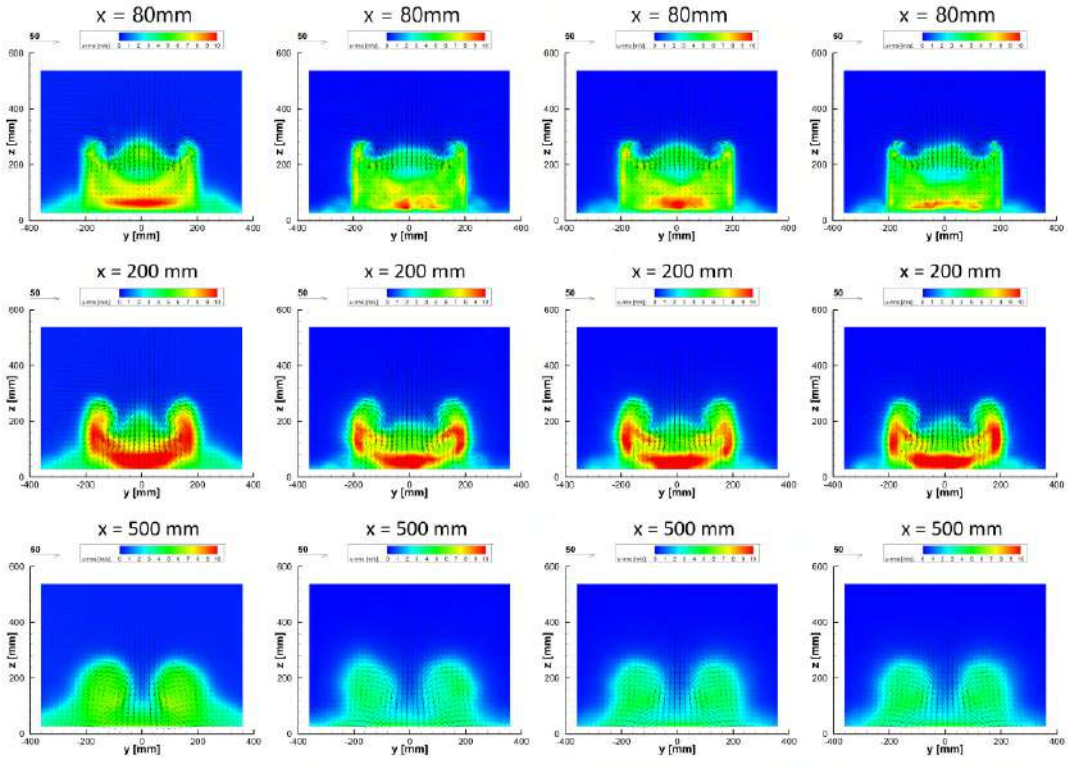

Figure 41: Contours of the average streamwise velocity fluctuations u-rms. From left to right: Exp., WMLES, IDDES, and PANS.

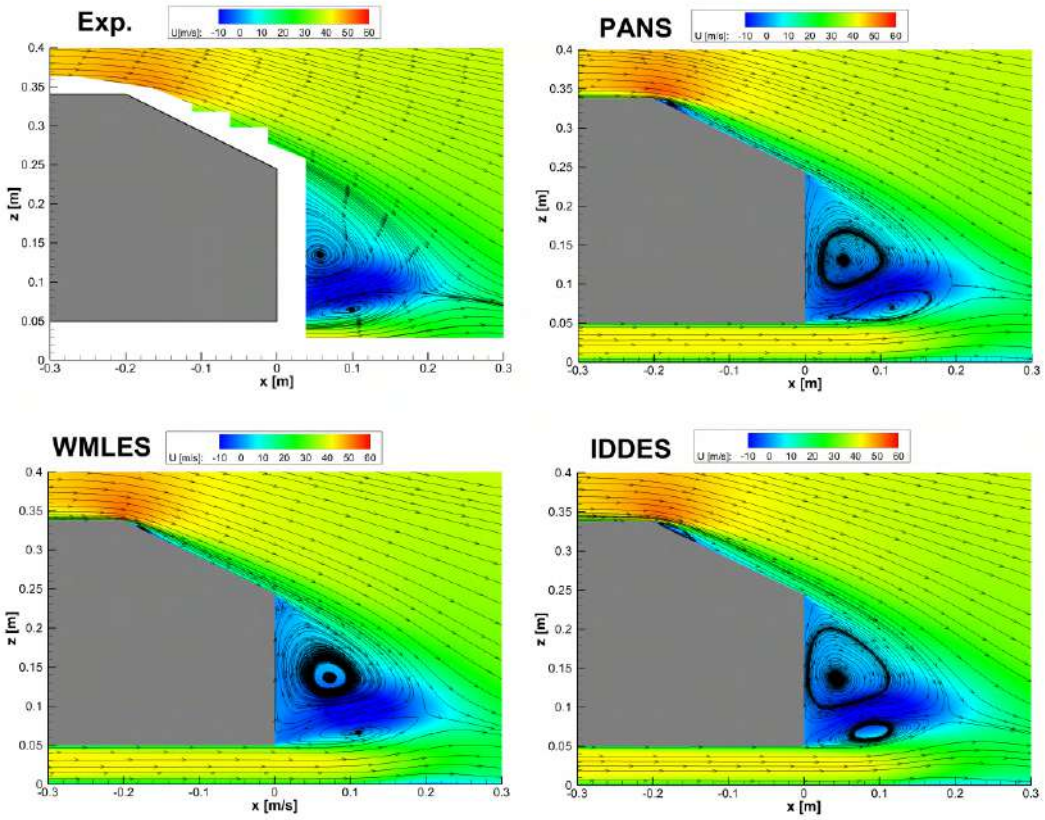

Figure 42: Contours of averaged wall shear stresses on the Ahmed body

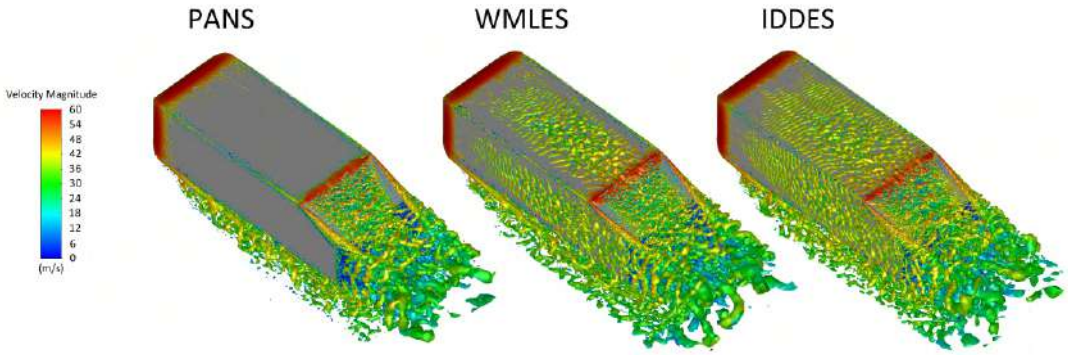

Figure 43: Isosurfaces of Q-criterion with contours of velocity magnitude

Chapter Six

Conclusion

The work performed in this study along with the main findings and conclusions are presented in this Chapter. The RANS one-equation model for the transport of turbulent eddy viscosity ν_t was transformed into an equation for the unresolved part of the turbulent eddy viscosity ν_{tu} in a PANS framework. As shown previously, this change of variables requires quantifying amount of modeling, thus a formulation for the ratio of unresolved-to-total eddy viscosity f_{ν_t} was derived from the energy density equation that maps the whole spectrum. Since integrating the energy spectrum would result in an equation for the unresolved-to-total turbulent kinetic energy f_k, the Bradshaw hypothesis was applied to switch from f_k to f_{ν_t}. The resulting formulation would be a function of the total turbulent eddy viscosity, thus requiring the solution of a RANS model. On the other hand, switching from ν_t to ν_{tu} as the main variable, would result in a complicated implicit formulation. It was shown, however, that using the energy spectrum for the large scales (inertial range) and adding a damping function for the smaller scales (high wavenumbers) would result in an adequate formulation for f_{ν_t}. The coefficient of the damping function was then calibrated to yield the correct near wall behavior for unresolved eddy viscosity. A UDF source code was developed to introduce the proposed transport equation in the numerical solver with the help of the ANSYS Fluent macros. The numerical simulation were setup to mimic the experimental setups, with several mesh densities considered for the backward facing step, and a very fine mesh for the Ahmed body. Sampling time studies were carried out for both the backward-facing step and Ahmed body cases to show time independence of the presented results. It was found that the first case requires at least 0.5s of sampling after transient effects have passed which is equivalent to around 1500 flow-through the step Height. The second case only required 0.24s or the

equivalent to 8 flow-through the body length. This will hopefully serve as reference for future works. The proposed model showed very good agreement with the experimental data for the backward-facing step. Although the c_f was slightly under-predicted for denser meshes after reattachment, the model was still able to accurately predict the reattachment length. It should be noted that both the WMLES and IDDES also showed this same c_f behavior with mesh refinement. Further investigation should be performed to check if this is a common issue in scale-resolving methods, or a result of the numerical settings used. Nevertheless, it was also shown that PANS with the proposed formulation is better able to predict velocity profiles and turbulent stresses. In addition, iso surface of the Q criterion revealed that in PANS more structures were resolved compared to the other scale-resolving models investigated. For the Ahmed body, the three models considered in this study i.e., WMLES, IDDES, and PANS, showed acceptable results, with PANS and IDDES having a modest advantage over WMLES. PANS was able to predict the closest lift coefficient and a better drag coefficient than the IDDES. For the velocity profiles, all models showed good agreement with the experiments, while velocity fluctuations were better predicted by PANS in some regions and IDDES in others. Overall, the proposed PANS model in this study showed good preliminary results. Being the first model to use only an equation for the unresolved turbulent eddy viscosity, a vast amount of is still required and large number of parameters to be investigated.

References

Ahmed, S. R., Ramm, G., & Faltin, G. (1984). Some salient features of the time-averaged ground vehicle wake. *SAE International*. https://doi.org/https://doi.org/10.4271/840300

Ansys fluent customization manual. (2019).

Ansys fluent theory guide. (2019).

Badri Narayanan, M. A., Khadgi, Y. N., & Viswanath, P. R. (1974). Similarities in pressure distribution in separated flow behind backward-facing steps. *Aeronautical Quarterly*, *25*(4), 305–312. https://doi.org/10.1017/s0001925900007095

Bradshaw, P., Ferriss, D. H., & Atwell, N. P. (1967). Calculation of boundary-layer development using the turbulent energy equation. *Journal of Fluid Mechanics*, *28*(3), 593–616. https://doi.org/10.1017/S0022112067002319

Chaouat, B. (2017). The state of the art of hybrid rans/les modeling for the simulation of turbulent flows. *Flow, Turbulence and Combustion*, *99*(2), 279–327. https://doi.org/10.1007/s10494-017-9828-8

Chaouat, B., & Schiestel, R. (2009). Progress in subgrid-scale transport modelling for continuous hybrid non-zonal rans/les simulations. *International Journal of Heat and Fluid Flow*, *30*(4), 602–616. https://doi.org/10.1016/j.ijheatfluidflow.2009.02.021

Davidson, P. A. (2000). Was loitsyansky correct? a review of the arguments. *Journal of Turbulence*, *1*, 6. https://doi.org/10.1088/1468-5248/1/1/006

Deardorff, J. W. (1970). A numerical study of three-dimensional turbulent channel flow at large reynolds numbers. *Journal of Fluid Mechanics*, *41*(2), 453–480. https://doi.org/10.1017/s0022112070000691

Driver, D., & Seegmiller, H. (1985). Features of a reattaching turbulent shear layer in divergent channel flow. *AIAA Journal*, *23(2)*, 163–171. https://doi.org/10.2514/3.8890

Fadai-Ghotbi, A., Friess, C., Manceau, R., & Jacques, B. (2010). A seamless hybrid rans-les model based on transport equations for the subgrid stresses and elliptic blending. *Physics of Fluids*, *22*(5), 055104. https://doi.org/10.1063/1.3415254

Falkovich, G., Gawedzki, K., & Vergassola, M. (2001). Particles and fields in fluid turbulence. *Reviews of Modern Physics*, *73*(4), 913–975. https://doi.org/10.1103/revmodphys.73.913

Foroutan, H., & Yavuzkurt, S. (2014). A partially-averaged navier–stokes model for the simulation of turbulent swirling flow with vortex breakdown. *In-*

ternational Journal of Heat and Fluid Flow, *50*, 402–416. https://doi.org/ https://doi.org/10.1016/j.ijheatfluidflow.2014.10.005

Girimaji, S. S. (2005). Partially-averaged navier-stokes model for turbulence: A reynolds-averaged navier-stokes to direct numerical simulation bridging method. *Journal of Applied Mechanics*, *73*(3), 413–421. https://doi.org/ 10.1115/1.2151207

Girimaji, S. S., & Abdol-Hamid, K. (2005). Partially-averaged navier stokes model for turbulence: Implementation and validation. *43rd AIAA Aerospace Sciences Meeting and Exhibit*. https://doi.org/10.2514/6.2005-502

Hinze, J. (1975). *Turbulence*. MCGRAW-HILL, Inc.

Huang, R., Luo, X., Ji, B., & Ji, Q. (2017). Turbulent flows over a backward facing step simulated using a modified partially averaged navier-stokes model. *Journal of Fluids Engineering*, *139*(4). https://doi.org/10.1115/1.4035114

Kolmogorov, A. N. (1968). Local structure of turbulence in an incompressible viscous fluid at very high reynolds numbers. *Soviet Physics Uspekhi*, *10*(6), 734–746.

Lesieur, M. (2014). *Turbulence in fluids*. Springer.

Lienhart, H., Stoots, C., & Becker, S. (2002). Flow and turbulence structures in the wake of a simplified car model (ahmed model). *Notes on Numerical Fluid Mechanics*, *77*. https://doi.org/10.1007/978-3-540-45466-3_39

Lilly, D. K. (1967). The representation of small-scale turbulence in numerical simulation experiments. *Proceedings of the IBM Science Computing Symposium on Environmental Science*, 195–210.

Ma, J. M., Peng, S. H., Davidson, L., & Wang, F. J. (2011). A low reynolds number variant of partially-averaged navier-stokes model for turbulence. *International Journal of Heat and Fluid Flow*, *32*(3), 652–669. https:// doi.org/10.1016/j.ijheatfluidflow.2011.02.001

Menter, F. R. (1997). Eddy viscosity transport equations and their relation to the k-ϵ*model*. *Journal of Fluids Engineering*, *119*(4), 876–884. https:// doi.org/10.1115/1.2819511

Menter, F. R. (2012). *Best practice: Scale-resolving simulations in ansys cfd*.

Murthi, A. (2004). *Effect of turbulent transport models and grid spacing on pans calculations of a lid-driven cavity (masters thesis)*.

Piomelli, U., Moin, P., & Ferziger, J. H. (1988). Model consistency in large eddy simulation of turbulent channel flows. *Physics of Fluids*, *31*(7), 1884. https: //doi.org/10.1063/1.866635

Reyes, D. (2008). *Partially averaged navier-stokes turbulence modeling: Investigation of computational and physical closure issues in flow past a circular cylinder (masters thesis).*

Schiestel, R., & Dejoan, A. (2005). Towards a new partially integrated transport model for coarse grid and unsteady turbulent flow simulations. *Theoretical and Computational Fluid Dynamics*, *18*(6), 443–468. https://doi.org/10.1007/s00162-004-0155-z

Serre, E., Minguez, M., Pasquetti, R., Guilmineau, E., Deng, G. B., Kornhaas, M., Schafer, M., Frohlich, J., Hinterberger, C., & Rodi, W. (2013). On simulating the turbulent flow around the ahmed body: A french-german collaborative evaluation of les and des. *Computers Fluids*, *78*, 10–23. https://doi.org/10.1016/j.compfluid.2011.05.017

Shur, M. L., Spalart, P. R., Strelets, M. K., & Travin, A. K. (2008). A hybrid rans-les approach with delayed-des and wall-modelled les capabilities. *International Journal of Heat and Fluid Flow*, *29*(6), 1638–1649. https://doi.org/10.1016/j.ijheatfluidflow.2008.07.001

Smagorinsky, J. (1963). General circulation experiments with the primitive equations. *Monthly Weather Review*, *91*(3), 99–164. https://doi.org/10.1175/1520-0493(1963)091⟨0099:gcewtp⟩2.3.co;2

Spalart, P., Strelets, M., Allmaras, S., & Jou, W. (1997). Comments on the feasibility of les for wings, and on a hybrid rans/les approach. *Conference: Advances in DNS/LES*.

Spalart, P. R., Deck, S., Shur, M. L., Squires, K. D., Strelets, M. K., & Travin, A. (2006). A new version of detached-eddy simulation, resistant to ambiguous grid densities. *Theoretical and Computational Fluid Dynamics*, *20*(3), 181–195. https://doi.org/10.1007/s00162-006-0015-0

Speziale, C. G. (1998). Turbulence modeling for time-dependent rans and vles: A review. *AIAA Journal*, *36*(2), 173–184. https://doi.org/10.2514/2.7499

Wang, B., Yang, Z., & Zhu, H. (2019). Active flow control on the 25° ahmed body using a new unsteady jet. *International Journal of Heat and Fluid Flow*, *79*, 108459. https://doi.org/10.1016/j.ijheatfluidflow.2019.108459